

## Boussinesq modeling of longshore currents

Qin Chen,<sup>1</sup> James T. Kirby,<sup>2</sup> Robert A. Dalrymple,<sup>3</sup> Fengyan Shi,<sup>2</sup> and Edward B. Thornton<sup>4</sup>

Received 16 January 2002; revised 20 June 2003; accepted 11 September 2003; published 26 November 2003.

[1] A time domain Boussinesq model for nearshore hydrodynamics is improved to obtain the conservation of vertical vorticity correct to second order and extended for use on an open coast using longshore periodic boundary conditions. The model is utilized to simulate surface waves and longshore currents under laboratory and field conditions. Satisfactory agreement is found between numerical results and measurements, including root mean square wave height, mean water level, and longshore current. One striking result of the simulations is the prediction of the strong longshore current in the trough shoreward of the bar as observed during the Duck Experiment on Low-frequency and Incident-band Longshore and Across-shore Hydrodynamics field campaign. The model results give insight into the spatial and temporal variability of wave-driven longshore currents and the associated vertical vorticity field under the phase-resolving, random wave forcing with wave/current interaction. Numerical experiments are carried out to examine the response of the modeled longshore currents to the randomness of surface waves and the cross-shore distributions of bed shear stress coefficient. We find that both regular and irregular waves lead to very similar mean longshore currents, while the input of monochromatic, unidirectional waves results in much more energetic shear waves than does the input of random waves. The model results favor *Whitford and Thornton's* [1996] finding that the bed shear stress coefficient for the area offshore the bar is larger than that in the trough, as better agreement with the field data for both regular and irregular waves is found if such coefficients are used in the Boussinesq model. *INDEX TERMS*: 4546 Oceanography: Physical: Nearshore processes; 4560 Oceanography: Physical: Surface waves and tides (1255); 4512 Oceanography: Physical: Currents; 4255 Oceanography: General: Numerical modeling; *KEYWORDS*: longshore currents, Boussinesq modeling, nearshore circulation, surf zone currents, wave breaking, irregular waves

**Citation:** Chen, Q., J. T. Kirby, R. A. Dalrymple, F. Shi, and E. B. Thornton, Boussinesq modeling of longshore currents, *J. Geophys. Res.*, 108(C11), 3362, doi:10.1029/2002JC001308, 2003.

### 1. Introduction

[2] The significant role of wave-induced longshore currents in coastal processes has long been recognized. Considerable research effort has therefore been devoted to the measurement and prediction of longshore currents generated by obliquely incident waves breaking near a shoreline. Since the pioneering work on modeling longshore currents by *Bowen* [1969], *Thornton* [1970], and *Longuet-Higgins* [1970a, 1970b], among others, a hierarchy of mathematical models has been established. Most of the existing models are based on the nonlinear shallow

water equations driven by the forcing of radiation stresses resulting from the averaging of the short wave field over the wave period. The simplest are one-dimensional (1-D) models based on the momentum flux balance in the longshore direction on a planar beach with a monochromatic incident wave train. The complexity and applicability of the models increase with the improved formulation of bottom shear stress and radiation stresses, the consideration of topographic variation in the longshore and cross-shore directions, and the introduction of the momentum dispersion mechanism resulting from vertical nonuniformities of the surf zone current. Obviously, the accuracy of each type of model depends on the quality of the wave transformation and breaking model that provides a mean flow model with the driving force. Reviews on advances in modeling longshore currents are given by *Basco* [1983], *Battjes et al.* [1991], and *Svendsen and Putrevu* [1995].

[3] On the basis of a gravity wave modeling technique introduced by *Abbott et al.* [1978], *Basco* [1983] suggested that time domain Boussinesq-type models resolving each individual wave in shallow water could become a superior alternative to wave-averaged models for the study of surf

<sup>1</sup>Department of Civil Engineering, University of South Alabama, Mobile, Alabama, USA.

<sup>2</sup>Center for Applied Coastal Research, University of Delaware, Newark, Delaware, USA.

<sup>3</sup>Department of Civil Engineering, Johns Hopkins University, Baltimore, Maryland, USA.

<sup>4</sup>Oceanography Department, Naval Postgraduate School, Monterey, California, USA.

zone currents. One of the advantages of Boussinesq models is that there is no need to decouple the wave and current motion [Chen *et al.*, 1998, 1999a], and thus no need to compute the radiation stresses for a separate run of a wave-averaged model. Furthermore, the capabilities of modeling nonlinear wave-wave interactions in shallow water and fully coupled wave-current interaction make the Boussinesq approach a promising tool for the study of low-frequency motions, including shear instabilities of longshore currents, if wave breaking is incorporated into the model.

[4] Significant advances in Boussinesq modeling of gravity wave transformation have been made over the past 5 ~ 10 years. Reviews on this subject were given by Kirby [1997] and Madsen and Schäffer [1999]. Recent progress in incorporating energy dissipation caused by wave breaking into time domain Boussinesq-type models by Karambas and Koutitas [1992], Schäffer *et al.* [1993], Svendsen *et al.* [1996], Veeramony and Svendsen [2000], and Kennedy *et al.* [2000], among others, allows for the prediction of breaking-induced nearshore circulation by averaging the modeled fluid particle velocity for the combined wave/current motion over a certain period of time. For example, Sørensen *et al.* [1998] and Chen *et al.* [1999b] have demonstrated the capabilities of Boussinesq-type models for the simulation of rip currents generated in the laboratory. However, few applications of two-dimensional (2-D) Boussinesq models to field conditions have been reported in the literature.

[5] The U.S. Army Engineering Waterways Experiment Station's Coastal and Hydraulic Laboratory Field Research Facility (FRF) located at Duck, North Carolina has served as the base of a series of nearshore field experiments [Birkemeier *et al.*, 1996]. These extensive field measurements not only significantly improve the understanding of complex phenomena in coastal processes, but also provide an excellent database for model verifications. On the other hand, numerical simulations of these data sets can lead to insight into the spatial and temporal variability of coastal dynamics, which can augment limited in situ observations. Also, a validated model will be useful for the planning of instrument deployment in the field.

[6] In this study, a time domain Boussinesq model for nearshore hydrodynamics, introduced by Wei *et al.* [1995] and Chen *et al.* [1999b], is improved to obtain vertical vorticity conservation correct to the second order, consistent with the order of approximation for the wave motion. This model is then used to investigate surface waves and longshore currents under controlled laboratory and uncontrolled field conditions. In section 2, we present the governing equations including additional terms to ensure the property of vorticity conservation followed by a summary of the features of the Boussinesq model, including shoreline runup, periodic lateral boundaries, multidirectional wave maker, wave breaking, bottom friction, and subgrid turbulent mixing. Section 3 describes the numerical simulation of wave-induced longshore currents measured by Visser [1991] in the laboratory with a planar beach. We examine the balance of momentum flux and the mechanism of momentum mixing predicted by the model. The numerical results are compared with the measured wave height, mean water level, and longshore current. In section 4, a data set obtained from the Duck Experiment on Low-frequency and

Incident-band Longshore and Across-shore Hydrodynamics (DELILAH) field experiment is simulated by the Boussinesq model. In addition to the model/data comparison of wave height and longshore current, we present the spatial and temporal variation of the computed wave-driven current field averaged over five peak wave periods, and the vorticity field obtained from the instantaneous velocity of the combined wave and current motion. Numerical experiments are carried out to examine the response of the modeled longshore currents to the spatial distributions of bed shear stress coefficient under both regular and irregular wave conditions. Finally, we summarize the findings in section 5.

## 2. Model Formulation

### 2.1. Governing Equations

[7] As Boussinesq-type models are extended into the surf zone, questions arise on the applicability of the equations for the breaking-generated, horizontal, rotational flow. A number of Boussinesq-type equations were derived under the assumption of irrotational flow [e.g., Wei *et al.*, 1995; Madsen and Schäffer, 1998]. Similar equations can also be derived from the Euler equations of motion [e.g., Yoon and Liu, 1989; Nwogu, 1993; Chen *et al.*, 1998], which allows for the advection of vertical vorticity. To bridge the equations originating from two different starting points of derivation, Wei *et al.* [1995] retained the leading-order vertical vorticity in their equations formulated in terms of velocity at a reference elevation and free surface elevation as the dependent variables, as shown by the vorticity transport equation by Chen *et al.* [1999b] and more recently by Liu [2000]. Starting from Euler equation on the free surface to avoid the evaluation of the pressure field, Gobbi *et al.* [2000] derive Boussinesq-type equations with the vertical vorticity consistent with the order of approximation for the wave motion. On the other hand, the study of horizontal vorticity in Boussinesq-type equations was reported by Rego and Neves [1997] and Veeramony and Svendsen [2000] who restricted their investigations to the vertical plane, and by Shen [2001], who dealt with a general three-dimensional case.

[8] Because a large number of Boussinesq models in use are based on the assumption of potential flow [see, e.g., Madsen and Schäffer, 1999], we demonstrate an alternative to Gobbi *et al.* [2000] to ensure vorticity conservation correct to the order of approximation of the equations by consistently introducing the vertical vorticity into the equations of irrotational flow.

[9] The three dimensional Euler equations on a Cartesian coordinate system can be written as

$$\frac{\partial \mathbf{u}}{\partial t} + \nabla_3 \left( \frac{1}{2} \mathbf{u} \cdot \mathbf{u} \right) + \boldsymbol{\Omega} \times \mathbf{u} + \frac{1}{\rho} \nabla_3 p + g \nabla_3 z = 0 \quad (1)$$

in which  $\mathbf{u} = (u, v, w)$  is the velocity vector at any location of the fluid domain,  $p$  is the pressure,  $\boldsymbol{\Omega} = \nabla_3 \times \mathbf{u}$  is the vorticity vector,  $t$  is time,  $\nabla_3$  is the three dimensional gradient operator,  $z$  is the vertical coordinate pointing upward with the origin on the still water surface,  $\rho$  is the fluid density, and  $g$  is the gravitational acceleration.

[10] Using Taylor expansion of the velocity about the still water surface and assuming zero horizontal vorticity, we

obtain the vertical distribution of the horizontal velocity vector,  $\hat{\mathbf{u}}$  [see, e.g., *Nwogu*, 1993],

$$\hat{\mathbf{u}} = \mathbf{u}_\alpha + \mu^2 \left\{ (z_\alpha - z) \nabla [\nabla \cdot (h\mathbf{u}_\alpha)] + \left( \frac{z_\alpha^2}{2} - \frac{z^2}{2} \right) \nabla (\nabla \cdot \mathbf{u}_\alpha) \right\} + O(\mu^4 \sqrt{gh_0}) \quad (2)$$

where  $\mathbf{u}_\alpha = (u_\alpha, v_\alpha)$  is the horizontal velocity vector at a reference elevation  $z_\alpha = -0.531h$  in the water column,  $h$  is the still water depth, and  $\nabla = (\frac{\partial}{\partial x}, \frac{\partial}{\partial y})$  is the horizontal gradient operator. Notice that  $\mu$  is the measure of wave dispersion and  $\mu = h_0/L < 1$  in shallow water, where the typical water depth  $h_0$  is smaller than the typical wavelength  $L$ . Depth integration of the continuity equation  $\nabla_3 \cdot \mathbf{u} = 0$  yields the vertical velocity

$$w = -\mu [z \nabla \cdot \mathbf{u}_\alpha - \nabla \cdot (h\mathbf{u}_\alpha)] + O(\mu^3 \sqrt{gh_0}) \quad (3)$$

Thus the vorticity vector  $\boldsymbol{\Omega}$  may be expressed as

$$\boldsymbol{\Omega} = \nabla_3 \times \mathbf{u} = (0, 0, \omega) \quad (4)$$

where the vertical component of the vorticity vector is

$$\omega = \frac{\partial v_\alpha}{\partial x} - \frac{\partial u_\alpha}{\partial y} + \mu^2 \omega_1 + O(\mu^4 \frac{\sqrt{gh_0}}{L}) \quad (5)$$

The second-order vertical vorticity is given by

$$\omega_1 = \frac{\partial z_\alpha}{\partial x} \left\{ \frac{\partial}{\partial y} [\nabla \cdot (h\mathbf{u}_\alpha)] + z_\alpha \frac{\partial}{\partial y} (\nabla \cdot \mathbf{u}_\alpha) \right\} - \frac{\partial z_\alpha}{\partial y} \left\{ \frac{\partial}{\partial x} [\nabla \cdot (h\mathbf{u}_\alpha)] + z_\alpha \frac{\partial}{\partial x} (\nabla \cdot \mathbf{u}_\alpha) \right\} \quad (6)$$

[11] The Euler equation in the vertical direction gives the pressure field as a function of  $z$

$$\begin{aligned} \frac{p}{\rho} = & g(\eta - z) + \mu^2 (z - \eta) \left\{ \nabla \cdot (h\mathbf{u}_{\alpha t}) + \frac{1}{2} (z + \eta) \nabla \cdot \mathbf{u}_{\alpha t} \right. \\ & + \mathbf{u}_\alpha \cdot \nabla [\nabla \cdot (h\mathbf{u}_\alpha)] + \frac{1}{2} (z + \eta) \mathbf{u}_\alpha \cdot \nabla (\nabla \cdot \mathbf{u}_\alpha) \\ & \left. - \nabla \cdot (h\mathbf{u}_\alpha) \nabla \cdot \mathbf{u}_\alpha - \frac{1}{2} (z + \eta) (\nabla \cdot \mathbf{u}_\alpha)^2 \right\} + O(\mu^4 g a_0) \end{aligned} \quad (7)$$

in which  $\eta$  is the free surface elevation relative to the still water level,  $a_0$  is the typical wave amplitude, and subscript  $t$  indicates partial differentiation with respect to time. Consequently, substitution of equations (2), (3), (4), and (7) into equation (1) and evaluation of the equation at  $z = z_\alpha$  lead to the Boussinesq-type momentum equation for the partially rotational motion as follows

$$\frac{\partial \mathbf{u}_\alpha}{\partial t} + (\mathbf{u}_\alpha \cdot \nabla) \mathbf{u}_\alpha + g \nabla \eta + \mu^2 (\mathbf{V}_1 + \mathbf{V}_2 + \mathbf{V}_3) = O(\mu^4 \frac{gh_0}{L}) \quad (8)$$

where  $\mathbf{V}_1$  and  $\mathbf{V}_2$  are the dispersive Boussinesq terms

$$\mathbf{V}_1 = \frac{z_\alpha^2}{2} \nabla (\nabla \cdot \mathbf{u}_{\alpha t}) + z_\alpha \nabla (\nabla \cdot (h\mathbf{u}_{\alpha t})) - \nabla \left[ \frac{\eta^2}{2} \nabla \cdot \mathbf{u}_{\alpha t} + \eta \nabla \cdot (h\mathbf{u}_{\alpha t}) \right] \quad (9)$$

$$\begin{aligned} \mathbf{V}_2 = & \nabla \left[ (z_\alpha - \eta) (\mathbf{u}_\alpha \cdot \nabla) (\nabla \cdot (h\mathbf{u}_\alpha)) + \frac{1}{2} (z_\alpha^2 - \eta^2) (\mathbf{u}_\alpha \cdot \nabla) (\nabla \cdot \mathbf{u}_\alpha) \right] \\ & + \frac{1}{2} \nabla \cdot \left[ (\nabla (h\mathbf{u}_\alpha) + \eta \nabla \cdot \mathbf{u}_\alpha)^2 \right] \end{aligned} \quad (10)$$

The additional term  $\mathbf{V}_3 = (V_3^{(x)}, V_3^{(y)})$  accounts for the second-order effect of the vertical vorticity, and may be written as

$$V_3^{(x)} = -v_\alpha \omega_1 \quad (11)$$

$$V_3^{(y)} = u_\alpha \omega_1 \quad (12)$$

In comparison with *Wei et al.*'s [1995] equations, the only difference is the introduction of  $\mathbf{V}_3$  because the leading-order vertical vorticity was retained in their equations. In fact, adding  $\mathbf{V}_3$  to *Wei et al.*'s momentum equation makes it identical to the equation derived by *Liu* [1994] using the velocity potential function. Taking the curl of equation (8) leads to the vorticity equation

$$\frac{\partial \omega}{\partial t} + \mathbf{u}_\alpha \cdot \nabla \omega = -\omega \nabla \cdot \mathbf{u}_\alpha + O(\mu^4 \frac{gh_0}{L^2}) \quad (13)$$

We notice that  $\omega$  depends on  $\mathbf{u}_\alpha$  and  $z_\alpha$  only and is depth uniform although  $\hat{\mathbf{u}}$  is a quadratic with the vertical coordinate  $z$ . Clearly, equation (8) conserves vertical vorticity with a leading-order error of  $O(\mu^4)$ , which is consistent with the level of approximation in the Boussinesq equations themselves.

[12] The mass conservation equation remains unchanged from the form by *Wei et al.* [1995], and is given by

$$\frac{\partial \eta}{\partial t} + \nabla \cdot \mathbf{M} = O(\mu^4 \sqrt{gh_0}) \quad (14)$$

where

$$\begin{aligned} \mathbf{M} = & (h + \eta) \left[ \mathbf{u}_\alpha + \mu^2 \left\{ \left( \frac{z_\alpha^2}{2} - \frac{1}{6} (h^2 - h\eta + \eta^2) \right) \nabla (\nabla \cdot \mathbf{u}_\alpha) \right. \right. \\ & \left. \left. + \left( z_\alpha + \frac{1}{2} (h - \eta) \right) \nabla (\nabla \cdot (h\mathbf{u}_\alpha)) \right\} \right] \end{aligned} \quad (15)$$

[13] In summary, fully nonlinear Boussinesq equations derived from the assumption of potential flow can be readily converted to equations that allow for the partially rotational flow with vertical vorticity. This is done by consistently adding the vertical components of  $\boldsymbol{\Omega} \times \mathbf{u}$  evaluated at the reference elevation to the momentum equation as demonstrated above. We shall utilize the enhanced momentum equation (8) and the mass equation (14) in the present study. Following *Wei et al.* [1995],

quasi fourth-order finite difference schemes are used to solve the governing equations.

## 2.2. Boundary Conditions

[14] To simulate breaking-generated longshore currents on an unbounded natural beach, the cross-shore lateral boundaries in the numerical model should remain transparent or open to the fluid motion, including surface waves and mean flows. Similar to the difficulties associated with the treatment of open boundaries in numerical models of storm surge and coastal ocean circulation, no technique is available for a Boussinesq model to achieve the real transparency of an open boundary under field conditions. In the present study, we choose alongshore periodicity to represent lateral cross-shore boundaries, assuming the wave-induced flow is dominated by the local forcing and the effect of the periodicity assumption is insignificant if the lateral boundaries are located far away from the area of interest. The numerical implementation of the periodic lateral boundary condition in the Boussinesq model includes solving a cyclic tridiagonal system of linear equations.

[15] A closed offshore boundary in combination with a sponge layer is implemented in the Boussinesq model to serve as the offshore nonreflective boundary. Input waves are then generated internally by the source function technique developed by *Wei et al.* [1999]. An extension of the technique is needed under the assumption of alongshore periodicity of cross-shore boundaries. In the case of simulating irregular waves, the distribution of wave directions in each frequency bin has to be adjusted to meet the requirement of alongshore periodic boundaries. Given a directional wave spectrum, we first divide the energy frequency spectrum into about 100 equal energy frequency bins. Then the energy direction spectrum for each frequency is split into 10~30 directional bins. The wave direction for each bin is determined on the basis of a longshore wave number decomposition for each frequency based on the longshore domain length, frequency and water depth.

[16] The swash zone on a beach is the interface of the seawater and the land. Following *Chen et al.* [2000], we treat the entire computational domain as an active fluid domain by employing an improved version of the slot technique for the simulation of wave runup given by *Kennedy et al.* [2000]. The equations for conservation of mass (equations (14) and (15)) becomes

$$\beta \frac{\partial \eta}{\partial t} + \nabla \cdot \mathbf{M} = 0 \quad (16)$$

where

$$\mathbf{M} = \Lambda(h_0 + \eta) \left[ \mathbf{u}_\alpha + \left( \frac{z_\alpha^2}{2} - \frac{1}{6}(h^2 - h\eta + \eta^2) \right) \nabla(\nabla \cdot \mathbf{u}_\alpha) + \left( z_\alpha + \frac{1}{2}(h - \eta) \right) \nabla(\nabla \cdot (h\mathbf{u}_\alpha)) \right] \quad (17)$$

in which  $\beta$  and  $\Lambda$  are two dimensionless multipliers introduced for the treatment of shoreline run up [*Kennedy et al.*, 2000].

## 2.3. Energy Dissipation

[17] Wave breaking, subgrid turbulent mixing, and the bottom shear stress serve as the agents of energy dissipation in the Boussinesq model. Parameterization is required to

model those dissipation mechanisms. The resultant equation for conservation of momentum (8) may be written as

$$\frac{\partial \mathbf{u}_\alpha}{\partial t} + (\mathbf{u}_\alpha \cdot \nabla) \mathbf{u}_\alpha + g \nabla \eta + \mathbf{V}_1 + \mathbf{V}_2 + \mathbf{V}_3 - \mathbf{R}_b - \mathbf{R}_s + \mathbf{R}_f = 0 \quad (18)$$

where the additional terms,  $\mathbf{R}_b$ ,  $\mathbf{R}_s$ , and  $\mathbf{R}_f$ , represent the effects of wave breaking, subgrid lateral turbulent mixing, and bottom friction, respectively.

[18] For the reason of simplicity, we adopt the momentum mixing scheme introduced by *Kennedy et al.* [2000] and *Chen et al.* [2000] for the modeling of energy dissipation caused by wave breaking in shallow water. The effectiveness of the model has been demonstrated by *Chen et al.* [1999b] in the simulation of a rip current system. The basic idea behind this breaking model is the addition of a momentum diffusion term to the Boussinesq-type equations with the diffusivity strongly localized on the front face of a broken wave. The empirical coefficient,  $\eta_r^{(D)}$ , that controls the onset of wave breaking in the *Kennedy et al.* model, varies between  $0.35\sqrt{gh}$  and  $0.65\sqrt{gh}$ . The lower limit of the empirical coefficient is found to be more suitable to bar/trough beaches while the upper limit gives optimal agreement for waves breaking on monotone sloping beaches.

[19] In comparison with the breaking schemes on the basis of the roller or horizontal vorticity concept [*Schäffer et al.*, 1993; *Veeramony and Svendsen*, 2000], the momentum diffusion model leads to a similar energy dissipation to that shown by *Svendsen et al.* [1996]. This similarity suggests that our breaking scheme be interpreted as a momentum mixing term resulting from the vertical nonuniformities of the horizontal velocity in a broken wave (the roller effect), rather than a simple turbulence closure.

[20] Following *Chen et al.* [1999b], a *Smagorinsky* [1963]-like subgrid turbulent mixing term is introduced in the momentum equations. This term is similar to the breaking term in form, but it has a totally different definition of eddy viscosity  $\nu_s$ . In contrast to the breaking term that only acts locally on the front face of a broken wave, the eddy viscosity of the subgrid mixing term is determined by the breaking-induced current field, which may extend outside the surf zone.

$$\nu_s = c_m \Delta x \Delta y \left[ (U_x)^2 + (V_y)^2 + \frac{1}{2}(U_y + V_x)^2 \right]^{\frac{1}{2}} \quad (19)$$

in which  $U$  and  $V$  are the velocity components of the time-averaged underlying current field,  $\Delta x$  and  $\Delta y$  are the grid spacing in the  $x$  and  $y$  directions, respectively, and  $c_m$  is the mixing coefficient with a default value of 0.25. In the course of simulation, we obtain the underlying flow field by averaging the instantaneous fluid particle velocity over about 2 ~ 5 peak wave periods and update the eddy viscosity owing to subgrid turbulence accordingly.

[21] The bottom shear stress is modeled by the quadratic law in terms of the velocity for the combined wave and current motion.

$$\mathbf{R}_f = \frac{f}{h + \eta} \mathbf{u}_\alpha |\mathbf{u}_\alpha| \quad (20)$$

where  $f$  is the bed shear stress coefficient. Unlike the momentum mixing terms for wave breaking and subgrid

turbulence, the bottom friction term does not conserve momentum. Instead, it serves as a sink of both energy and momentum. Care has been taken when choosing the bed shear stress coefficients for modeling alongshore currents. The value of the friction coefficient varies in a wide range as found in the literature. Under field conditions, owing to the variability of hydrodynamic and morphologic characteristics, spatially variable friction coefficients on the order of  $f \approx 1.0 \times 10^{-3} \sim 5.0 \times 10^{-3}$  are likely to occur, as shown by *Whitford and Thornton* [1996] and *Feddersen et al.* [1998], who inferred the bed shear stress coefficients for longshore currents over a barred profile on the basis of momentum balance in the longshore direction. In the present study, we utilize both constant and spatially varying friction coefficients for field applications.

### 3. Simulation of *Visser's* [1991] Experiment

#### 3.1. Model Setup

[22] The measurements from a series of laboratory experiments on breaking-generated longshore currents on plane beaches were reported by *Visser* [1991]. This data set has served as a standard test of longshore current models [e.g., *Smith et al.*, 1993; *Svendsen and Putrevu*, 1994; and *Kobayashi et al.*, 1997]. We chose case 4 in *Visser's* [1991] experiments to demonstrate the capability of the wave-resolving Boussinesq-type model for the simulation of the stationary longshore current. In the physical model, the slope of the smooth concrete beach is 1:20, which starts from an offshore water depth of 35 cm. The obliquely incident, regular wave train has an amplitude of 0.39 cm, a period of 1.02 s, and an angle of incidence of 15.4 degrees in the offshore depth.

[23] The computational domain is chosen to be 12 m onshore and 5.6 m alongshore. We determine the width of the domain on the basis of the periodic lateral boundary condition. A 2.6 m flat bottom is placed in front of the slope. Waves are generated internally near the toe of the beach. A sponge layer is used in front of the offshore boundary to absorb the outgoing wave energy. The grid increments in the cross shore and longshore directions are chosen to be 0.03 m and 0.06 m, respectively, and the time step is 0.0102 s. We choose the bottom shear stress coefficient as  $f = 0.007$  by tuning the model to match the measurement.

#### 3.2. Model/Data Comparison

[24] The Boussinesq model is run for a duration of 150 waves and a stationary current is obtained. Figure 1 illustrates the computed wave field and the phase-averaged current field at the end of the simulation. It is seen from Figure 1a that the modeled wave crest becomes narrow and asymmetric near the shoreline owing to nonlinear shoaling effects. Depth-limited breaking reduces the wave height near the shoreline. We obtained the breaking-generated current by time averaging the computed fluid particle velocity over two wave periods of the regular wave train. The computed mean flow field is longshore uniform and no shear instabilities occur even as we increase the alongshore length of the computational domain and the simulation time. A stability analysis of the measured longshore current using *Putrevu and*

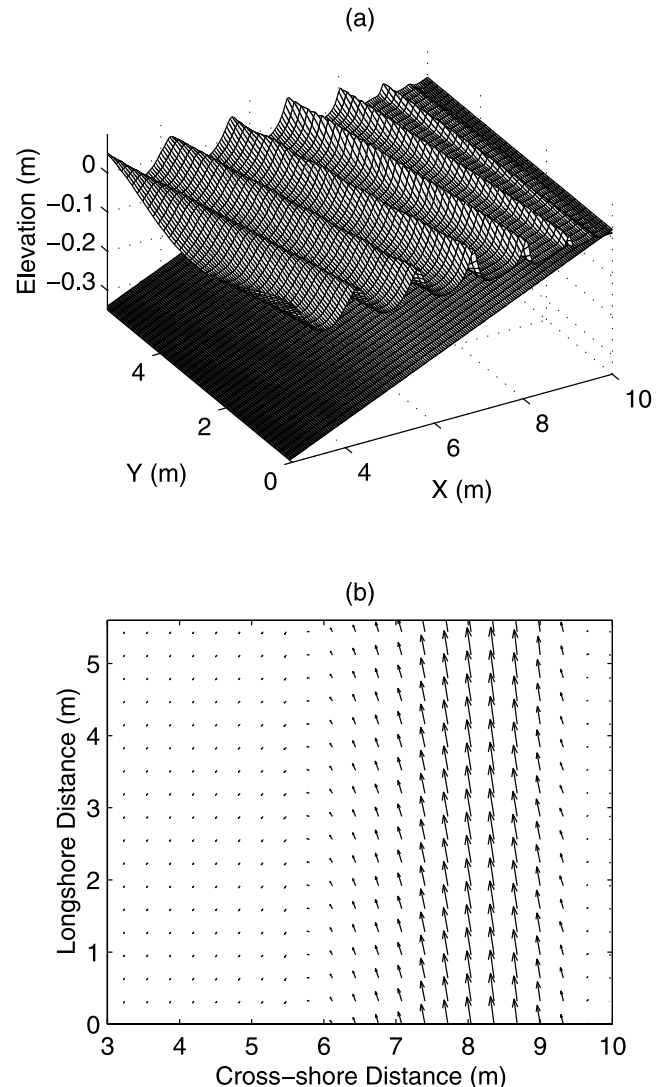


**Figure 1.** A snapshot of (a) the computed wave field with bathymetry and (b) the phase-averaged current field of case 4 in *Visser's* experiment.

*Svendsen's* [1992] method confirms that the current is linearly stable. A similar laboratory experiment with a nonbarred beach (test SC219) by *Reniers and Battjes* [1997] also indicated that shear instabilities are absent under this particular laboratory condition. The Boussinesq model predicts a weak cross-shore velocity, which is the return flow caused by Stokes' drift. Notice that the undertow is absent in the present model, as would be expected since the mass balance does not explicitly identify a roller contribution.

[25] Figure 2a depicts the cross-shore profiles of the computed longshore current at  $t = 20, 50, 100, 120$  s, respectively. We notice that the longshore current develops and reaches the steady state fairly rapidly. For instance, the longshore current reaches 85% of its maximum from a cold start after 50 waves break. A steady solution of the longshore current is achieved at the end of simulation as the profiles at  $t = 100$  s and 120 s are not distinguishable.

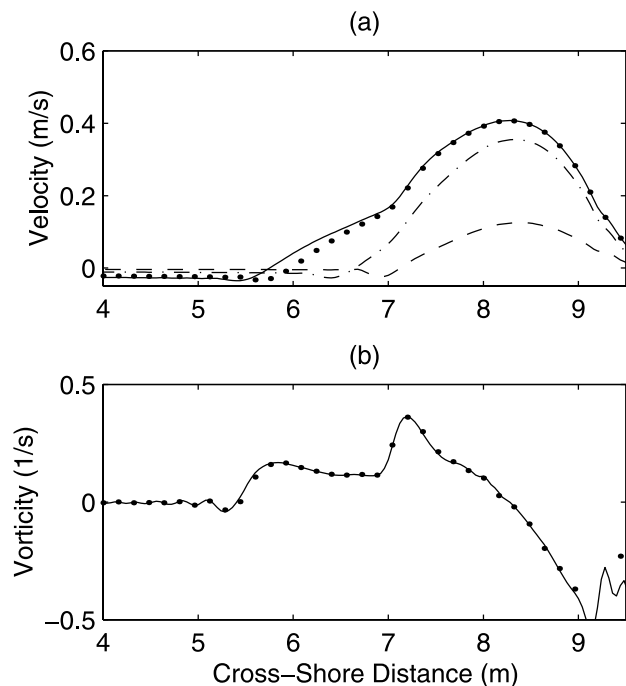


**Figure 2.** Cross-shore profiles of (a) the computed longshore currents at  $t = 20$  s (dashed line), 50 s (dash-dotted line), 100 s (dotted line), and 120 s (solid line) and (b) the vorticity obtained from the mean current (solid line) and the instantaneous fluid particle velocity (dotted line).

[26] The cross-shore distribution of the associated vertical vorticity is shown in Figure 2b. The solid line represents the vertical vorticity computed from the longshore current while the dotted line is obtained from the instantaneous fluid particle velocity. Apparently, they are identical. This again confirms that the gravity wave motion is basically irrotational while wave breaking provides the mean flow with the source of vorticity, as suggested by *Chen et al.* [1999b]. Owing to the longshore uniformity of the underlying current field, the effect of the vorticity correction introduced in section 2 vanishes in this case.

[27] Comparisons of the model results with the measurements are presented in Figure 3 where cross-shore variations of wave height, mean water level, and longshore current are shown. The circles are the data measured by *Visser* [1991] and the solid lines are the computed results. First, the Boussinesq model predicts a breaking location at  $x = 7$  m which is close to the measured initiation of wave breaking in the laboratory. The model, however, underpredicts the energy dissipation rate, overpredicting the wave height in the surf zone. Second, the agreement between the modeled and measured wave setup is fairly good. A delay of the elevated mean water level away from the breaking point is correctly simulated by the model. The slight underestimate of the wave setup may be partly attributed to underprediction of the energy dissipation rate by the model.

[28] As shown in Figure 3c, the modeled longshore current agrees with the measurement, including the magnitude and the location of the maximum velocity as well as the variation. The correct prediction of the cross-shore

distribution of the current indicates that the breaking scheme designed for energy dissipation due to wave breaking not only dissipates the wave energy fairly well, but also diffuses the longshore momentum flux correctly, similar to the roller effect. The mechanism of momentum mixing shall be discussed further in the next subsection.

### 3.3. Momentum Balance and Mixing

[29] In order to gain insight into the flow system predicted by the Boussinesq model, we examine the momentum balance and the diffusivity of the momentum mixing terms for wave breaking and subgrid turbulence. It is well known that a steady longshore current on a planar beach results from the balance between the cross-shore gradient of longshore momentum flux ( $S_{yx}$ ) owing to the short wave motion and the longshore component of the bottom shear stress ( $\tau_y$ ), i.e.,

$$\frac{\partial S_{yx}}{\partial x} = -\tau_y \quad (21)$$

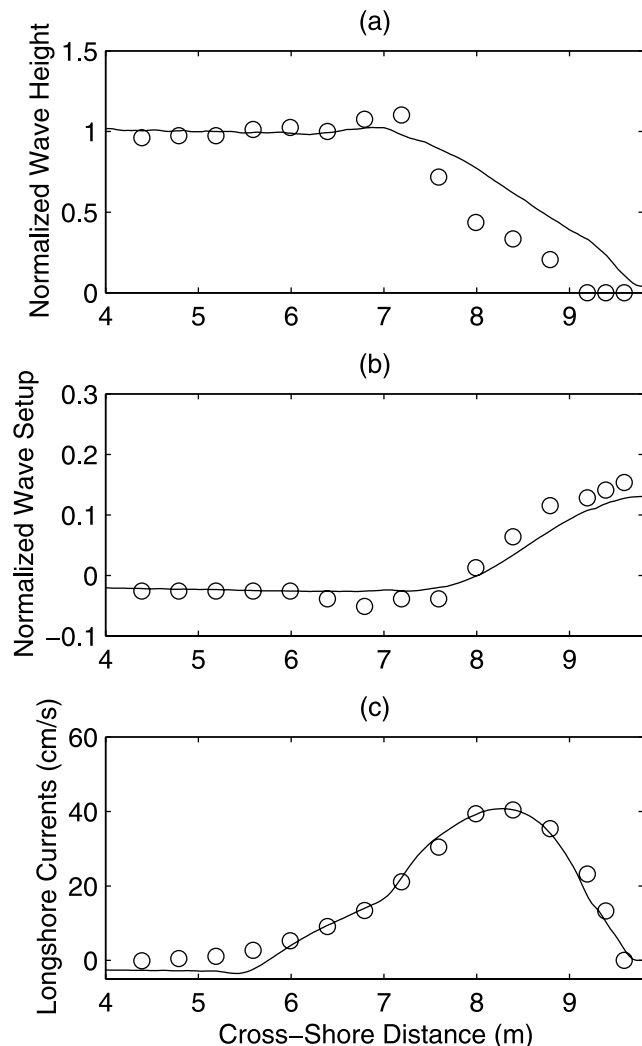


**Figure 3.** Comparison of computational results (solid lines) and measurements (circles): (a) wave height, (b) mean water level, and (c) longshore current.

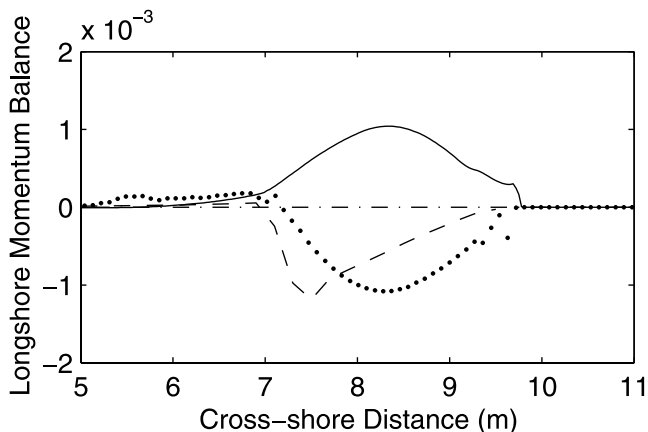


**Figure 4.** Alongshore momentum balance: solid line, the bottom friction; dotted line, the cross-shore gradient of the radiation shear stress  $\left(\frac{\partial S_{yx}}{\partial x}\right)$  given by the Boussinesq model; and dashed line,  $\frac{\partial S_{yx}}{\partial x}$  given by REF/DIF.

[30] By definition [see *Longuet-Higgins and Stewart, 1961*], the radiation shear stress is given by

$$S_{yx} = \overline{\int_{-h}^{\eta} \rho v u \, dz} \quad (22)$$

where the horizontal velocity ( $u, v$ ) is given by equation (2). We compute the radiation stresses using the instantaneous fluid particle velocity with the subtraction of the mean current averaged over two wave periods for regular waves or over five peak periods for irregular waves. The bottom shear stress is obtained by  $\tau_y = \rho(h + \bar{\eta})\bar{R}_{fy}$ , where the overbars denote a time average.

[31] Figure 4 shows the balance of wave-averaged momentum flux in the longshore direction described by equation (21). The dotted line represents the radiation stress evaluated using equation (22) and the modeled velocity that includes the effect of momentum diffusion owing to wave breaking. In contrast, a traditional estimate of radiation stresses using linear wave theory does not balance the bed shear stress predicted by the Boussinesq model, as shown by the dashed line in Figure 4 where the REF/DIF model [Kirby, 1986] is employed. Obviously, use of the conventional calculation of radiation stresses on the basis of the kinematics of linear waves would require a momentum mixing, or diffusion term in equation (21) in order to correctly predict the cross-shore distribution of a longshore current.

[32] The magnitude of momentum diffusion owing to wave breaking may be estimated by extracting the wave-averaged diffusivity of the momentum mixing terms from the model results. Figure 5a presents the eddy viscosity corresponding to wave breaking and the subgrid turbulence computed by the model [see *Chen et al., 1999b*]. Apparently, the diffusivity varies across the surf zone and wave breaking significantly dominates the momentum mixing inside the surf zone. The eddy viscosity resulting from the subgrid turbulence extends to the area seaward of the breaking line, i.e.,  $x = 5 \sim 7$  m, where the diffusivity

owing to wave breaking is zero, but it is very weak in comparison to the diffusivity inside the surf zone.

[33] *Svendsen* [1987] estimated the typical value of the breaking-generated turbulent eddy viscosity as  $0.01h\sqrt{gh}$  on the basis of laboratory experiments. Field measurement by *George et al.* [1994] suggested a reduction of *Svendsen's* estimate by 1/2 to 1/4 under field conditions. To compare with the previously estimated turbulent eddy viscosity, we divide the computed eddy viscosity by  $h\sqrt{gh}$ , as shown in Figure 5b. Apparently, the normalized eddy viscosity inferred from the Boussinesq model has a maximum of 0.04 in the inner surf zone, which is larger than the typical value of 0.01 estimated by *Svendsen* [1987]. This can be attributed to the additional diffusion similar to the roller effect.

## 4. Modeling DELILAH Longshore Currents

### 4.1. Topography and Model Setup

[34] A comprehensive field data collection campaign was conducted at U.S. Army Engineering Waterways Experiment Station, Coastal and Hydraulic Laboratory, Field Research Facility in October 1990. An overview of this project known as DELILAH was given by *Birkemeier et al.* [1997]. Among many interesting findings, DELILAH measurements indicate that the maximum longshore current could appear in the trough of a barred beach, which contradicts the conventional notion of longshore currents on alongshore uniform barred beaches, where a current maxi-

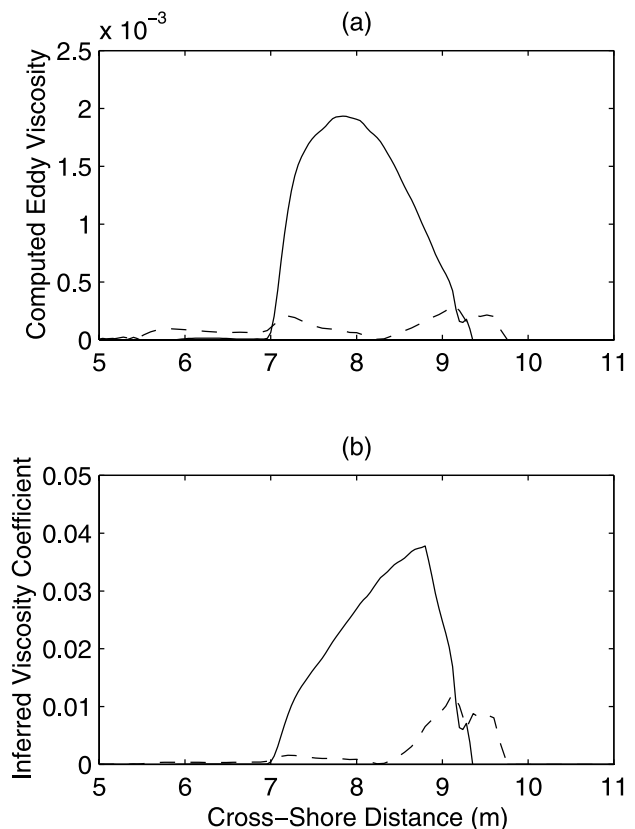


**Figure 5.** (a) Computed eddy viscosity and (b) the inferred viscosity coefficient. Solid line, the contribution from wave breaking; and dashed line, the contribution from subgrid turbulence.

imum is expected at the bar crest. A great deal of effort [e.g., *Smith et al.*, 1993; *Church and Thornton*, 1993; *Svendsen et al.*, 1997; *Reniers*, 1999] in the literature has been made to interpret and model the longshore currents observed during the DELILAH field experiment. The unsuccessful predictions of the occurrence of the maximum velocity in the trough by one-dimensional models suggest that it is important for the longshore current model to take into account the alongshore nonuniformities in the bathymetry [e.g., *Putrevu et al.*, 1995; *Reniers*, 1999; *Slinn et al.*, 2000]. In contrast to the modeling of longshore currents, the significant role of bathymetric variations in rip current generation has long been recognized since *Bowen* [1970] and *Dalrymple* [1978], among others.

[35] In the present study, we construct the 2-D bathymetry for the Boussinesq model on the basis of the survey data in the so-called minigrad area collected daily by the FRF staff during the DELILAH experiment. The daily surveyed area covers about 550 m in the longshore direction and 400 m offshore from the shoreline. To extend the bathymetry to the location near the 9-gage array in the 8-m water depth where the multidirectional waves were measured, we create a hybrid of the minigrad survey data and the offshore portion of the monthly survey data that covered the 8-m array. This is justified because *Birkemeier et al.* [1997] found that most of the bathymetric changes occurred in the minigrad area where the offshore movement of the inner bar was substantial.

[36] Figure 6 illustrates the topography of the model based on the daily survey data on 10 October 1990. The model covers an area of about 1 km<sup>2</sup> and the coordinates follow the FRF system. To construct the periodic cross-shore boundaries for the simulation of waves and currents on an open coast, we modify the south cross-shore boundary by extending the domain from  $y = 700$  m to  $y = 150$  m with a linear transition to the beach profile at the north cross-shore boundary. Notice that the model does not include the cross-shore bathymetric depression beneath the FRF pier because no daily survey data is available in that area. The alongshore length of the model is chosen to be 1,168 m. There are two reasons for making this choice. First, a larger model length will allow for a better representation of the discrete directional spreading function satisfying the periodic lateral boundary condition. Second, a large distance from the upstream boundary to the area of interest will significantly reduce the effect of errors introduced at the upstream boundary [*Chen and Svendsen*, 2003].

[37] A close examination of the bathymetry shows that there were two oblique ridges in the trough of the barred beach. This is clearly seen by following the 1 m contour in Figure 6b. Notice that the dashed line represents the primary cross-shore array transect of electromagnetic current meters and pressure sensors, which were deployed between the two oblique ridges.

[38] The model covers 900 m in the cross-shore direction, including the dry beach. In the offshore area with an artificial flat bottom, a source for the generation of directional, random waves is placed along the break of the slope. We use a 100 m wide sponge layer in front of the offshore boundary to absorb the outgoing waves. The grid increment is 1.5 m in the cross-shore direction and 4 m in the longshore direction. The time step is 0.107 s.

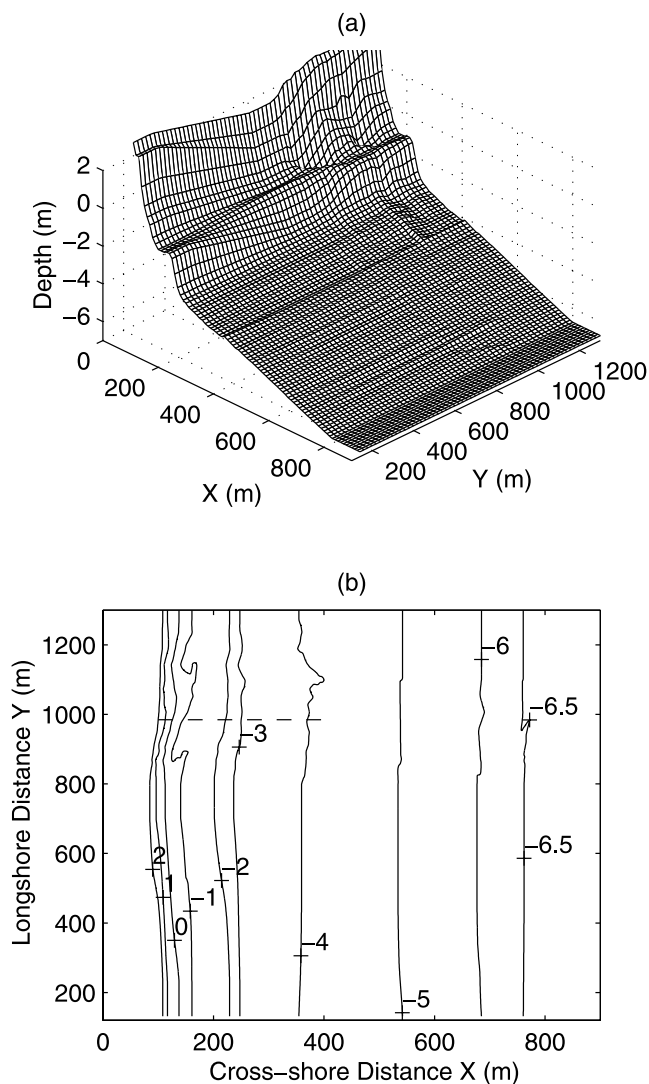


**Figure 6.** The barred beach of the model: (a) topography and (b) contours of still water depth. Dashed line: instrument transect.

[39] We select the low tide ( $-0.26$  m) at 03:51 AM on 10 October 1990 because waves are more likely to break seaward of the bar crest in comparison with the high tide condition, thus providing a more critical test with respect to the observed strong longshore current in the trough. Simulating this data set is a challenge because neither the 1-D model [*Church and Thornton*, 1993] nor the 2-D model [*Svendsen et al.*, 1997] predicted the correct location of the measured maximum longshore current. The measured incoming waves at the 8-m array had a root mean square wave height  $H_{rms} = 0.8$  m and a peak wave period  $T_p = 10.7$  s. The peak angle of the directional spectrum ( $\theta_p$ ) is  $-35$  degrees, which means the waves came from the southeast. In the literature, most of the 2-D longshore current models [e.g., *Wu et al.*, 1985; *Svendsen et al.*, 1997] use  $H_{rms}$ ,  $T_p$ , and  $\theta_p$  as the representative of the short wave field. The source function technique [*Wei et al.*, 1999] allows us to approximately reproduce the measured directional wave spectrum in the Boussinesq model. For the

reason of simplicity and flexibility, however, we utilize both a regular wave input and a TMA shallow water wave spectrum [Bouws *et al.*, 1985] with a wrapped normal directional spreading function [Borgman, 1984] as a parameterized directional spectrum in the present study.

[40] The dimensionless parameters,  $\delta$  and  $\lambda$ , controlling the width of the slot and the smoothness of the transition to the slot for the treatment of the moving shoreline [Kennedy *et al.*, 2000], are chosen to be 0.01 and 20, respectively. Considering the relative coarse resolution for high-frequency waves in the surf zone with the barred bathymetry, we select the lower limit of the breaking criterion (i.e.,  $\eta_r^{(D)} = 0.35\sqrt{gh}$ ) for the breaking scheme [see Kennedy *et al.*, 2000; Chen *et al.*, 2000]. The default coefficient  $c_m = 0.25$  is used for the subgrid turbulent mixing scheme.

[41] Whitford and Thornton [1996] suggested that bed shear stress coefficients decrease in magnitude shoreward, varying from  $f = 0.004 \pm 0.0013$  for offshore the bar to  $f = 0.001 \pm 0.0003$  in the trough. In contrast, Feddersen *et al.* [1998] suggested that bed shear stress coefficients inside the surf zone could be three times larger than those outside the surf zone. In the literature, spatially constant coefficients are often used in the modeling of longshore currents owing to the uncertainty in the actual cross-shore distribution, albeit inhomogeneous hydrodynamic and morphologic conditions in the field. To understand the response of the Boussinesq model to the cross-shore distribution of bed shear stress coefficient, we use three different types of distribution.

[42] 1. For type 1,  $f = 0.001$  for the water depth less than 1.5 m and  $f = 0.003$  for the water depth greater than 2.0 m with a linear variation between them. The distribution of bottom friction coefficient in this case mimics the conclusions of Whitford and Thornton [1996], based on the Superduck field experiment.

[43] 2. In contrast to type 1, type 2 has a spatially constant friction coefficient of  $f = 0.001$  for the water depth deeper than 2.0m and an increasing coefficient as the water depth decreases. The variation of the friction coefficient inside the surf zone follows the Manning-Strickler equation [e.g., Ruessink *et al.*, 2001]. This distribution leads to a larger bottom friction coefficient inside the surf zone, similar to the result of Feddersen *et al.* [1998] based on the Duck 94 field experiment.

[44] 3. For type 3:  $f = 0.0015$  over the entire computational domain.

[45] The time domain Boussinesq model resolves the phases of surface wave motion and needs a much finer grid size than that required by a phase-averaged model for the wave-driven flow. On the other hand, a longshore current needs a few hundred waves to build up to its full strength from a cold start in the field. We run the Boussinesq model for 214 min of simulation time that covers about 1,200 peak wave periods. The average of the last 120 min (673 peak wave periods) of the modeled results are used for model/data comparisons. We shall present the computed longshore current driven by a regular wave train followed by the model results of irregular waves.

#### 4.2. Model Results: Regular Waves

[46] A monochromatic, unidirectional wave train with the measured  $H_{rms}$ ,  $T_p$  and peak angle of incidence is generated using the source function technique. Figure 7 illustrates a

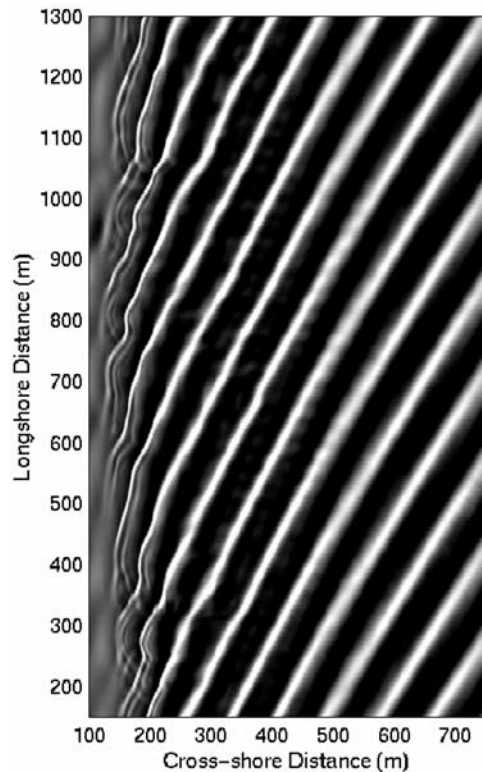


**Figure 7.** A snapshot of the computed free surface elevation at FRF: light areas represent the crests of the monochromatic wave field.

snapshot of the modeled free surface elevation at time  $t = 5350$  s. The wave crests are shown by the gray areas. We notice that, when the long-crested waves approach the shoreline, they become rather peaky because of the nonlinear shoaling effects. Refraction of the wave field by the sloping beach is also visible, as the wave angle decreases when the waves approach the shoreline.

[47] By time averaging the computed fluid particle velocity over the last 673 peak wave periods (120 min) of the simulation, we obtain the breaking-generated mean longshore current. The velocity is located at the reference level  $z_\alpha = -0.531h$  in the water column. Figure 8 shows the velocity vector field of the modeled mean current. Clearly, the longshore current is not alongshore uniform. Instead, it meanders between  $y = 900$  m  $\sim$  1300 m, which corresponds to the two oblique ridges in the trough and the longshore variation of the barred bathymetry. Notice that the 120-min averaging process smooths out the shear wave features to be discussed later.

[48] The comparison of the modeled root mean square wave height and the mean longshore current with the field measurements is shown in Figure 9 where the beach profile is also presented as a reference. The solid lines are the model results while the circles are the measurements averaged over 120 min from 03:51 on 10 October 1990. As seen in Figure 6b, the cross-shore transect of the primary array in the DELILAH experiment is located at  $y = 986$  m. In general, good agreement between the model results and the measured data is found when type 1 bottom friction coefficient is used.

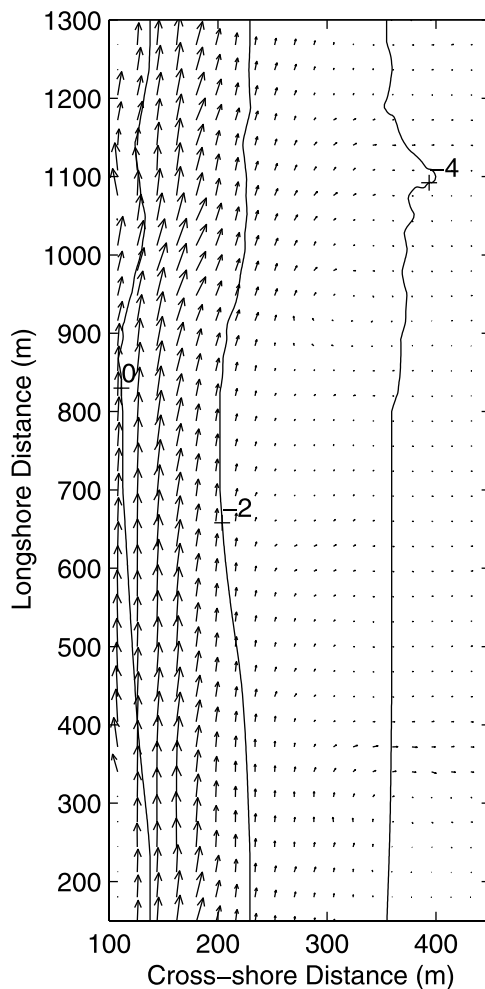


**Figure 8.** Time-averaged longshore current at FRF. The solid lines represent the contours of the still water depth.

[49] First, nonlinear wave shoaling and refraction are predicted well by the Boussinesq model as shown by the good agreement of the wave height outside the surf zone. The breaking location that is seaward of the bar crest is also captured by the model. Inside the surf zone, the energy dissipation rate is slightly underpredicted by the model and the cessation of wave breaking in the trough is not as apparent as the measurement indicates. The model predicts that strong wave breaking occurs again near the shoreline, which is in agreement with the observation. Second, it is seen in Figure 9b that the computed cross-shore distribution of the longshore current agrees with the measurement. For comparison, the dashed line in Figure 9b illustrates the result given by *Church and Thornton's* [1993] 1-D model. Obviously, the 1-D model fails to predict both the location and magnitude of the maximum longshore current. The Boussinesq model, however, overpredicts the magnitude of the longshore current on the bar crest.

[50] The model results with the bottom friction coefficients of types 2 and 3 are shown in Figure 10. It is seen that the spatial distributions of friction coefficient virtually do not affect the agreement of the modeled wave height and the measurement inside the surf zone. The modeled wave

height outside the surf zone and longshore currents, however, are sensitive to the spatial distributions of friction coefficient. The Boussinesq model with both types 2 and 3 distributions tends to underpredict the magnitude of the longshore current in the trough, and significantly overestimate the current strength outside the surf zone. Owing to wave/current interaction, the overpredicted longshore current outside the surf zone significantly affects the shoaling waves, as shown in Figure 10b. Apparently, the Boussinesq model favors a larger friction coefficient outside the surf zone under this particular field condition, similar to the result of *Whitford and Thornton* [1996] based on the

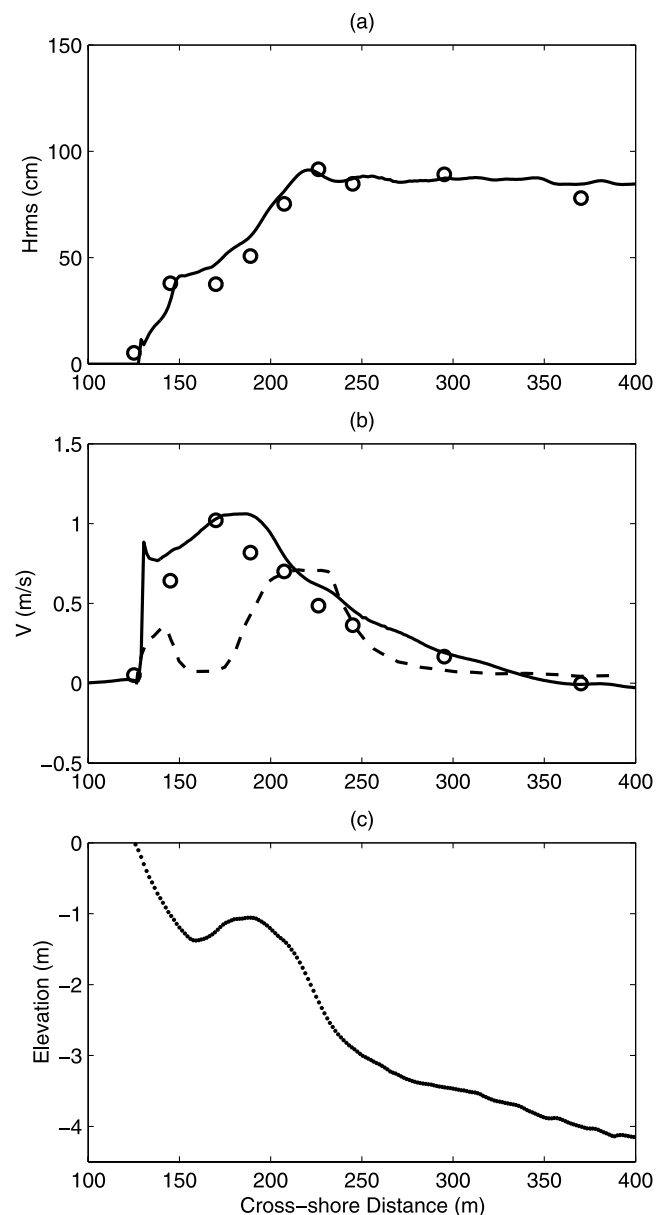


**Figure 9.** Comparisons of the computational results and the field measurements in the case of regular waves and type 1 bottom friction: (a) root mean square wave height, (b) cross-shore distribution of longshore current, where the dashed line depicts the solution of the 1-D model given by *Church and Thornton* [1993], and (c) beach profile.

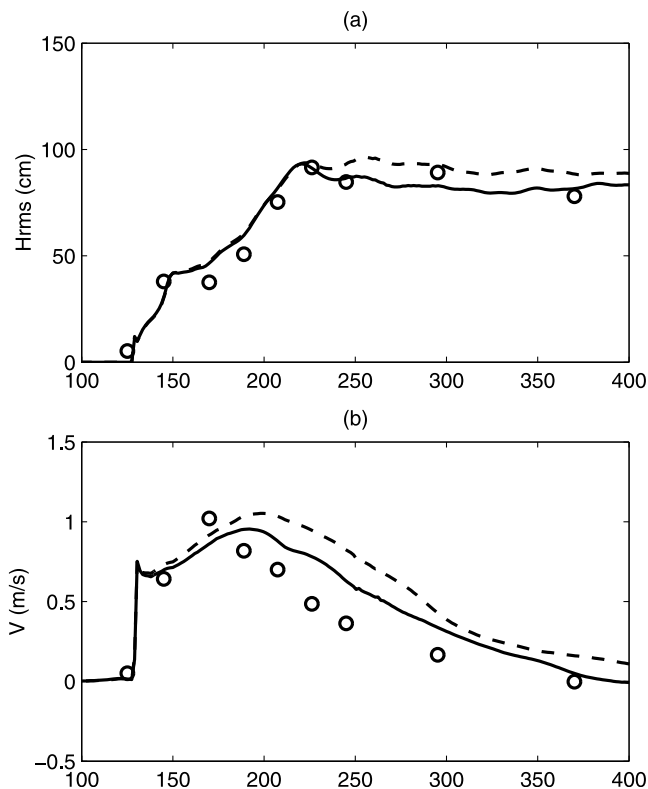


**Figure 10.** Comparisons of the computational results and the field measurements in the case of regular waves: (a) root mean square wave height and (b) cross-shore distribution of longshore current. Solid lines, type 2 of  $f$ ; dashed lines, type 3 of  $f$ ; and circles, measurements.

Superduck field experiment. However, this may not hold for other field conditions because hydrodynamic and morphological conditions could be different.

[51] The nonlinear dynamics of finite amplitude shear instabilities of longshore currents have been studied by Allen *et al.* [1996], Slinn *et al.* [1998], Özkan-Haller and Kirby [1999], and Slinn *et al.* [2000], among others using the nonlinear shallow water equations with stationary wave forcing. Similarly, the results of the time domain Boussinesq model provide information on the spatial and temporal variabilities of the wave-driven currents. Figure 11 presents a time sequence of the modeled longshore current and the associated vorticity field at  $t = 202, 206, 210,$  and  $214$  min, approximately, with type 1 friction coefficient. The longshore current is obtained by averaging the computed fluid particle velocity over 5 peak wave periods to filter out the short wave motion. On the other hand, we calculate the vertical vorticity using the instantaneous velocity for the combined wave and current motion to avoid smoothing out the vorticity field, as shown in the lower panels. Obviously, both approaches give very similar vorticity fields. It is seen that the longshore current meanders and the flow pattern changes with time. There are strong vortices associated with the current field. Formation of the vortices is triggered by nonlinear shear instabilities, and possibly bathymetric variations. In comparison with the vorticity field in the upper panels, the instantaneous vorticity field reveals more detailed features of the flow, such as the signature of wave

breaking in the surf zone and more rapid spatial variation of the vorticity field.

[52] As indicated by the transport equation of the vertical vorticity [Chen *et al.*, 1999b], the instantaneous vorticity is advected by the fluid particle velocity at the reference elevation  $z_{\omega}$ , including the wave orbital velocity and the underlying current that is dominant. Following the presentation style used by Özkan-Haller and Kirby [1999], Figure 12 shows the computed vorticity in the trough ( $x = 170$  m) and seaward of the bar crest ( $x = 225$  m) as a function of longshore distance and time. The streaks of the bright areas illustrate the peaks of the vorticity waves while the blue colors denote the troughs of the vorticity waves. As an example, the bottom panels show the time series of the vorticity at  $y = 1000$  m in the trough and seaward of the crest, respectively. The sampling frequency of the instantaneous vertical vorticity is  $1/5$  the peak wave frequency. Notice that the slope ( $\frac{dx}{dt}$ ) of each streak represents the alongshore propagation speed of the corresponding shear wave. The shear waves in the trough contain much more energy in the high-frequency band than in the shear waves seaward of the bar crest. It is seen that larger amplitude shear waves (i.e., stronger vorticity) propagate more slowly than smaller amplitude shear waves. This is consistent with Özkan-Haller and Kirby's [1999] finding about the dependency of the shear wave speed on the shear wave amplitude. The time-averaged celerity of the shear waves at the location of  $(x, y) = (170, 1000)$  m is about  $1.0 \text{ ms}^{-1}$ , which is very close to the speed of the local mean current. The maximum speed of the computed mean longshore current at that cross-shore profile is about  $1.1 \text{ ms}^{-1}$ , while the local shallow water wave celerity is about  $3.3 \text{ ms}^{-1}$ .

### 4.3. Model Results: Irregular Waves

[53] Figure 13 depicts the representative directional spectrum, which is narrow banded in both frequency and directional spreading. The parameter controlling the broadness of the TMA spectrum [Bouws *et al.*, 1985] is  $\gamma = 5.0$ , and the angular standard deviation of the directional spreading function [Borgman, 1984] is  $\sigma_{\theta} = \pi/18$ . In comparison with the measured directional spectrum provided by the FRF staff, the chosen TMA spectrum is rather narrow banded. There are two reasons for making such a choice. First, the grid size and time step are selected to best resolve the wave component at the peak of the energy spectrum within the computational limit. Thus wave components in the high-frequency band of a broad frequency spectrum will not be sufficiently resolved in the model. Second, the width of the computational domain is chosen on the basis of the alongshore periodicity of the cross-shore boundaries with respect to the peak angle of the directional spectrum. Consequently, the angles of wave incidence in a broad directional spectrum may not be well represented in the model. A sensitivity test of the incident wave condition is carried out. The model results indicate that a broader directional spectrum with  $\gamma = 3.3$ , and  $\sigma_{\theta} = \pi/9$  leads to similar agreement with the measurements of wave height and mean longshore current as does the input of the chosen narrow banded spectrum.

[54] We divide the representative directional spectrum into 1800 components with random phases and transform them into a time series using the source function technique

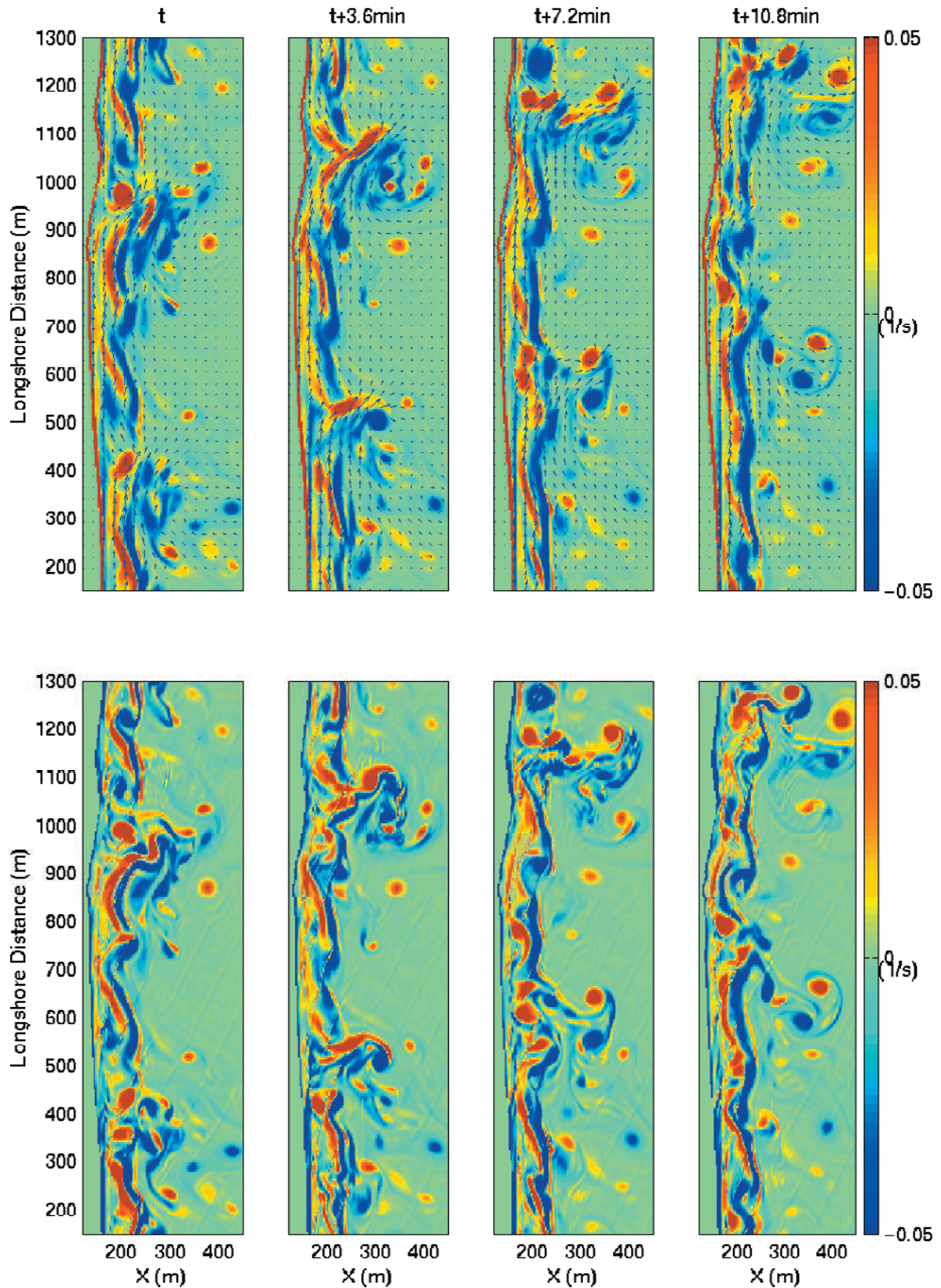


**Figure 11.** Time sequence of the vorticity field. (top) Velocity vectors and vorticity field averaged over 5 peak wave periods and (bottom) instantaneous vorticity field. The faint diagonal streaks are the individual wave crests.

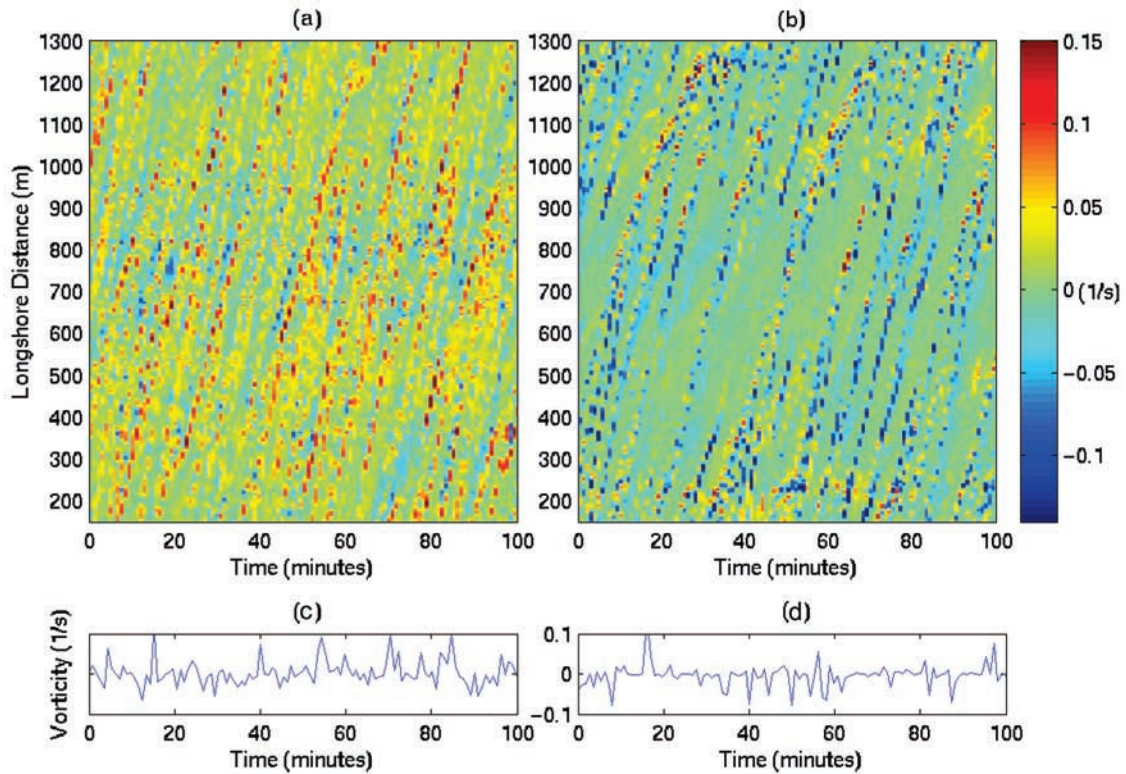


**Figure 12.** (a) Contour plot of vorticity as a function of time and longshore distance in the trough and (b) seaward of the bar crest and (c) time series of vorticity at the measurement array in the trough and (d) seaward of the crest.

extended to a longshore periodic domain. Unlike wave models in the frequency domain, simulating hundreds of wave components in the time domain Boussinesq model does not lead to notable increase in the computational time in comparison with the case of a single wave component. Figure 14 illustrates a snapshot of the modeled water surface elevation at time  $t = 5350$  s. The wave crests are shown by the lighter gray areas. In contrast to Figure 7, the input of the TMA directional spectrum leads to a random, short-crested wave field.

[55] Figure 15 shows a comparison of the modeled root mean square wave height and the mean longshore current with the field measurements, where the beach profile is also presented as a reference. The solid lines are the model results with type 1 bottom friction coefficient, while the circles are the measurements averaged over 120 min. It is seen in 15a that though the energy dissipation rate inside the surf zone is underpredicted, the breaking model captures the breaking location correctly. Compared with the case of regular waves, poorer agreement with the data in the case of random waves suggests that finer spatial resolution is needed in order to resolve high-frequency waves in the trough. In spite of the discrepancy in wave height, Figure 15b shows that the computed longshore current still agrees with the measurements fairly well. The Boussinesq model predicts a very strong current shoreward of the bar crest, which is absent in the 1-D model shown by the dashed line. Similar to the case of regular waves, the velocity seaward of the bar crest is overpredicted. This is probably attributed to the smaller bottom drag coefficient ( $f = 0.001$ )

on the bar crest used in the model than that in *Whitford and Thornton* [1996] ( $f = 0.003$ ).

[56] The response of the computed longshore current to the bed shear stress coefficients of types 2 and 3 is shown in Figure 16. Similar to the results of regular waves, both types of coefficient lead to overpredictions of the longshore current velocity offshore the bar and underpredictions of the velocity in the trough compared with the measurements. The predicted wave height, however, is barely affected by

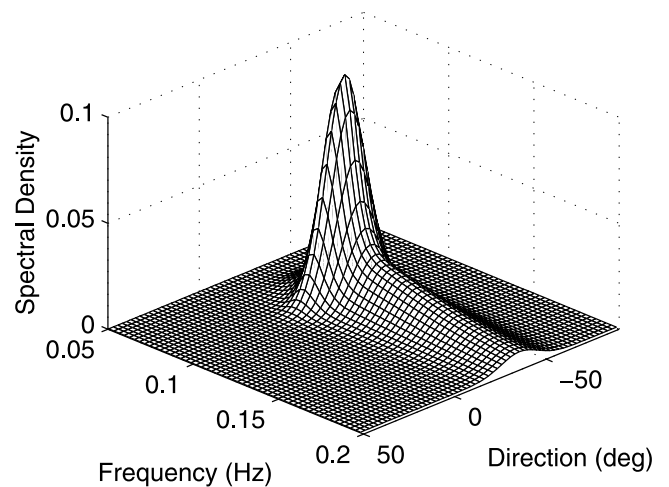


**Figure 13.** A narrow-banded directional spectrum. The unit of the spectral density is  $\frac{m^2}{deg Hz}$ .

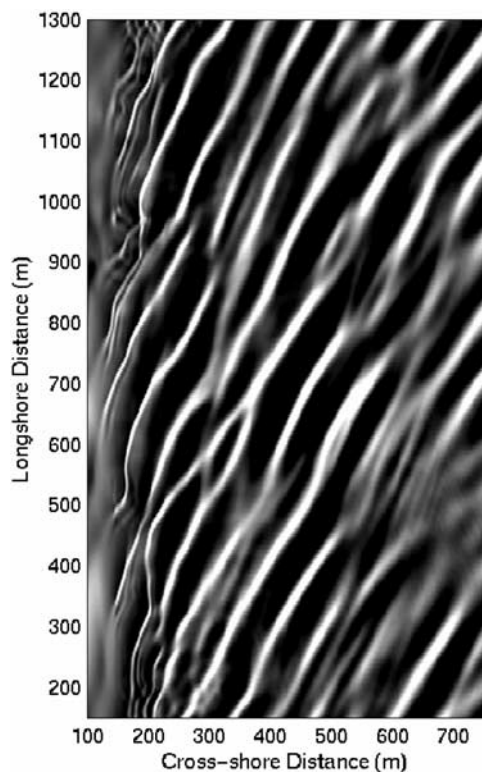


**Figure 14.** A snapshot of the computed free surface elevation at FRF: light areas represent the wave crests of the narrow-banded wave field.

the different cross-shore distributions of friction coefficient in the case of random waves except in the offshore area where the strength of the longshore current is considerably overpredicted. Consistent with the results of regular waves, the Boussinesq model favors type 1 friction coefficient under the DELILAH field conditions with random waves.

[57] To test the sensitivity of longshore currents to the randomness and directional spreading of input waves, we choose a broader TMA spectrum that mimics the measured directional spectrum obtained from the measurements at the FRF 8-m array at 4:00 AM on 10 October 1990 [Birkemeier *et al.*, 1997]. The parameter controlling the broadness of the TMA spectrum  $\gamma = 3.3$ , and the angular standard deviation of the directional spreading function  $\sigma_\theta = \pi/9$ . A snapshot of the computed water surface is shown in Figure 17. It is seen that the wave field is more short crested and realistic in this case compared to Figure 14. Again, perfect alongshore periodicity is achieved in this random wave field with broad frequency and directional spreading. The bed shear stress coefficient of type 1 is used.

[58] Figure 18 shows snapshots of the computed instantaneous vorticity fields in the case of random waves, corresponding to both the narrow-banded (top) and broad-banded (bottom) spectra. Each snapshot of vertical vorticity field is taken 3.6 min apart, starting from  $t = 202$  s, in both cases. First, the signature of wave crests is visible in the instantaneous vorticity field. Outside the surf zone, the faint diagonal streaks are the weak vertical vorticity generated by the bed shear stress under individual wave crests. Inside the surf zone, the energy dissipation

term localized on the wave front provides the source of vorticity. The injection of vorticity by the individual random breakers is likely to produce shear waves that are different from those driven by the conventional, phase-averaged forcing on the basis of the nonlinear shallow water equation and a separate wave model. Second, we notice that the shear waves in both the random wave cases are less energetic than those generated by the monochromatic waves as shown in Figure 11. The random waves, on the other hand, tend to result in more shear wave energy in the high-frequency band than does a monochromatic, unidirectional wave train. Because the focus of the

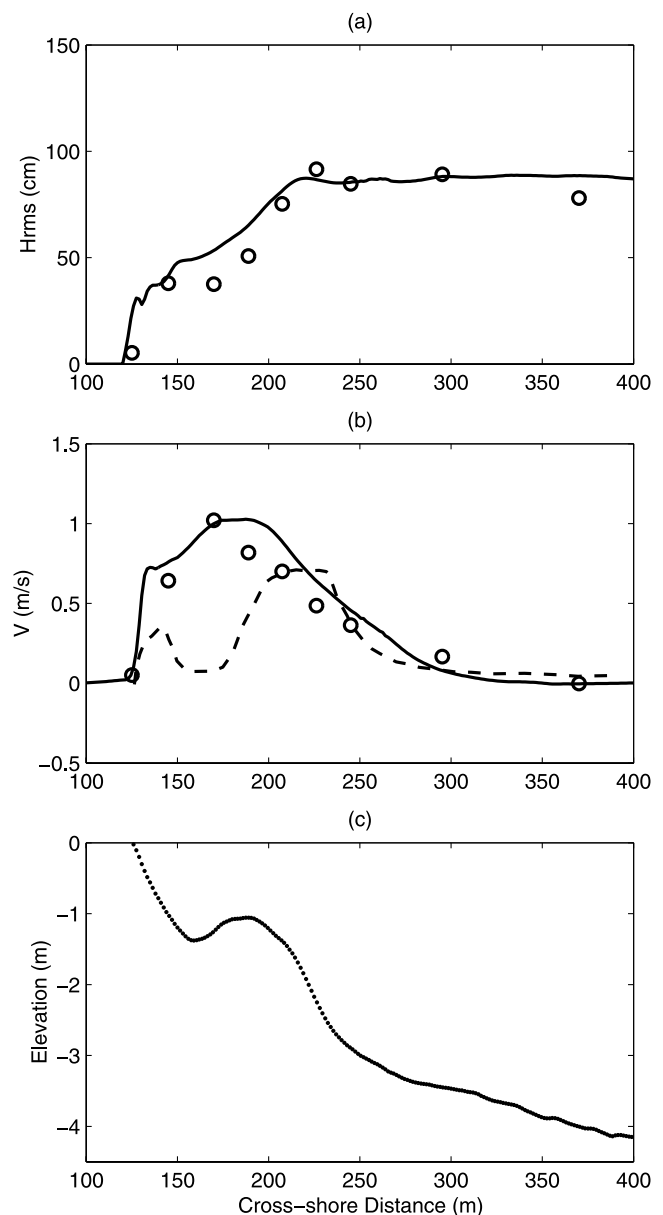


**Figure 15.** Comparisons of the computational results and the field measurements in the case of a narrow-banded spectrum: (a) root mean square wave height, (b) cross-shore distribution of longshore current, where the dashed line depicts the solution of the 1-D model given by Church and Thornton [1993], and (c) beach profile.

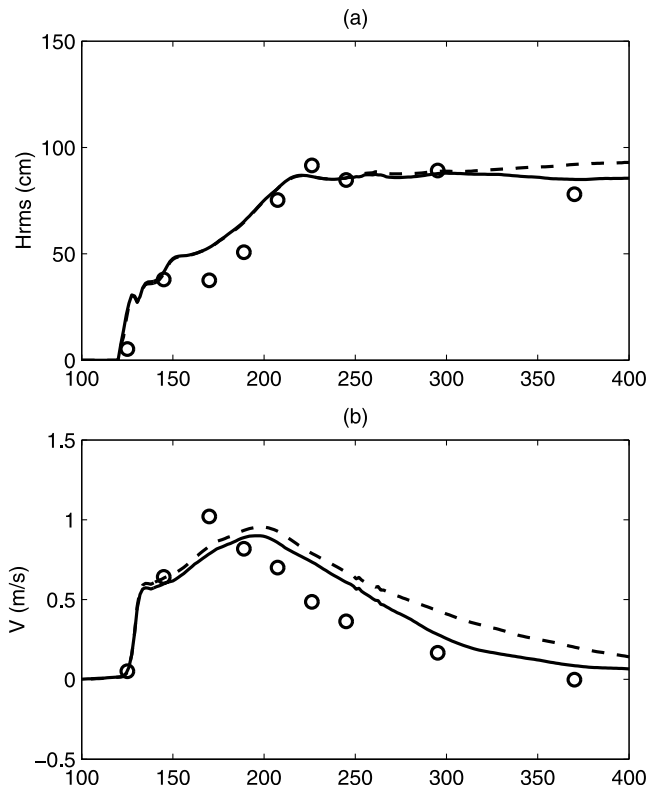


**Figure 16.** Comparisons of the computational results and the field measurements in the case of a narrow-banded spectrum: (a) root mean square wave height and (b) cross-shore distribution of longshore current. Solid lines, type 2 of  $f$ ; dashed lines, type 3 of  $f$ ; and circles, measurements.

present study is mean longshore currents, we leave the detailed statistical and spectral analyses of the shear waves or vorticity for future investigation in conjunction with the simulation of the Sandyduck data set. Preliminary results have been presented by Kirby *et al.* [2002].

[59] The effect of the wave randomness and directional spreading on the modeled longshore currents is illustrated in Figure 19 where the solid, dot-dashed, and dashed lines respectively denote the results of monochromatic, narrow-banded, and broad-banded surface waves. It is seen in Figure 19a that both random wave cases result in very similar agreement with the measured wave height, while the monochromatic, unidirectional wave train leads to somewhat better agreement with the data. The comparison of the mean longshore currents generated by different surface wave fields is shown in Figure 19b. The broad-banded spectrum leads to a slightly weaker maximum longshore current than those in the other two cases. Despite the significant difference in the driving force provided by the three different surface wave fields, the resultant longshore currents are very similar in comparison with the measured longshore current. This contradicts the predictions of 1-D models based on the balance of momentum flux in the alongshore direction. As a random wave field with broader frequency and directional spreading has smaller radiation stresses integrated over the whole spectrum [e.g., Ruessink *et al.*, 2001], such 1-D models would predict a weaker longshore current than that generated by the corresponding

monochromatic, unidirectional waves if the lateral mixing and bed shear stress coefficient are kept unchanged.

[60] Though we use an identical bed shear stress coefficient for these three simulations, the degree of lateral mixing varies because of the differences in the resultant shear waves. Figure 19c compares the standard deviations of the instantaneous vertical vorticity, or the amplitudes of the shear waves at the nine gage locations under these three surface wave conditions. It turns out that the monochromatic, unidirectional waves lead to a much more energetic shear wave field than those generated by random waves. Thus stronger lateral mixing is expected in the regular wave case.

## 5. Summary and Conclusions

[61] In this study, the fully nonlinear Boussinesq equations derived by Wei *et al.* [1995] are improved to include the vertical vorticity consistent with the order of approximation for the wave motion. A brief description of the treatments of boundary conditions and energy dissipation in the time domain Boussinesq model is given with an emphasis on the extension of the model to an open coast. We validate this extended Boussinesq model against the Visser's [1991] laboratory experiment on longshore currents over a planar beach. Reasonable agreement is found between the numerical and physical model results, including wave height, mean water level, and longshore current. An analysis of the momentum flux balance predicted by the Boussinesq model suggests that the momentum mixing due to the breaking scheme incorporated in the present model is

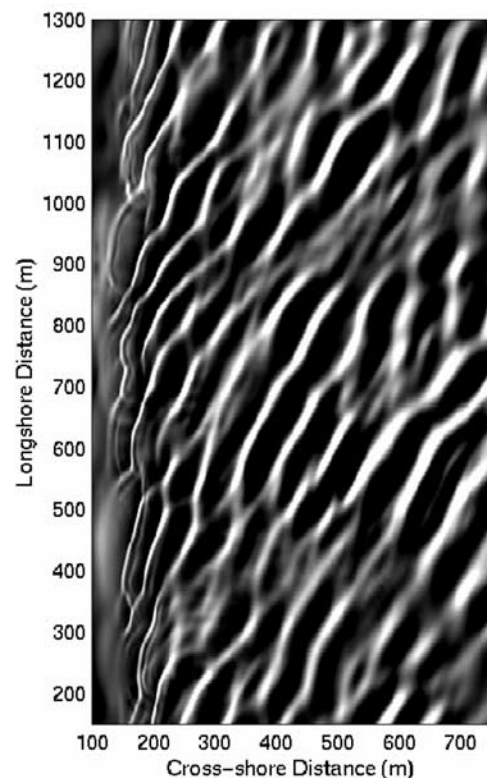


**Figure 17.** A snapshot of the computed free surface elevation at FRF: light areas represent the wave crests of the random wave field with a broader directional spectrum.

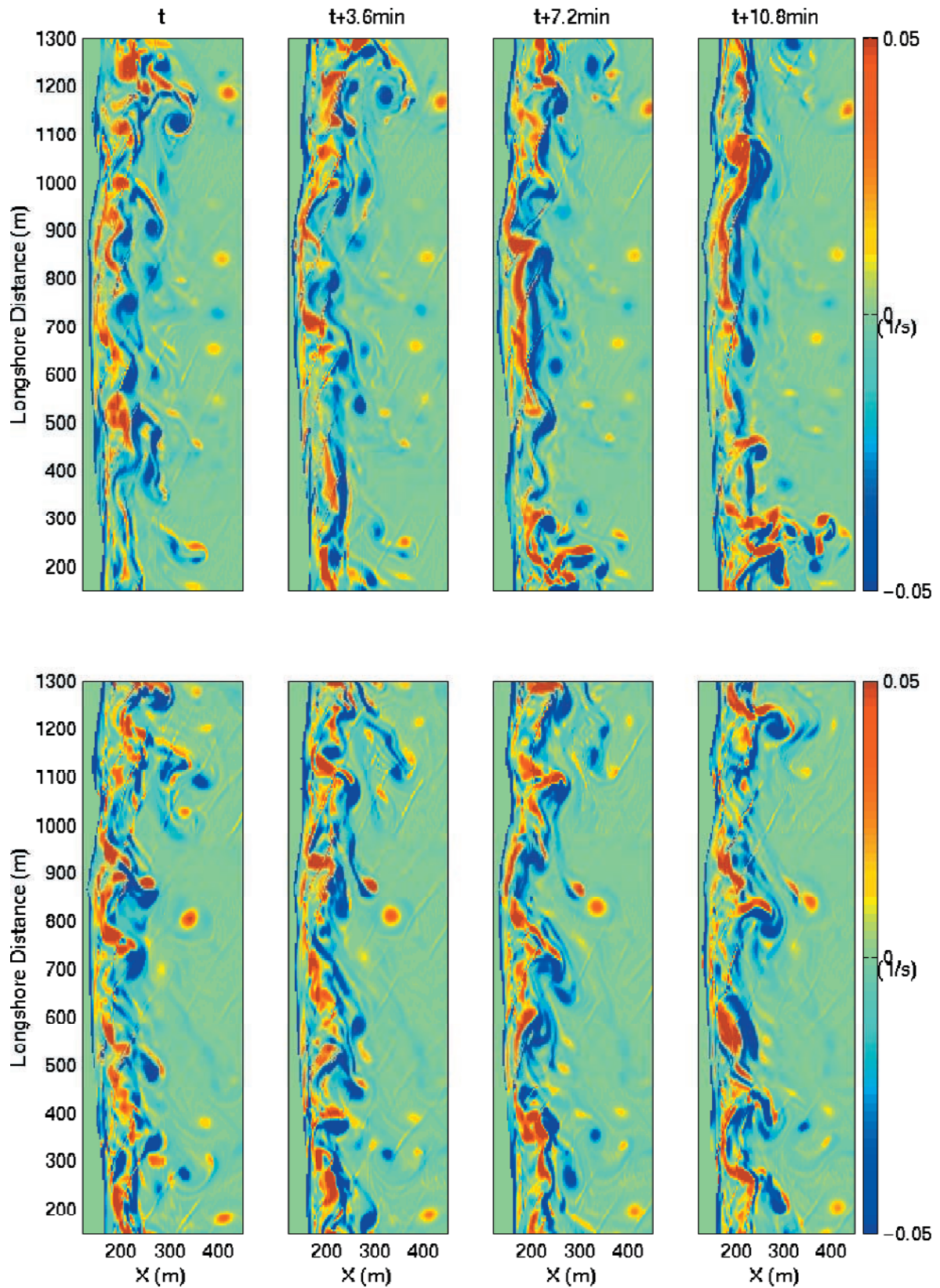


**Figure 18.** Time sequence of the instantaneous vorticity fields. (top) A narrow-banded spectrum and (bottom) a broadbanded spectrum. The faint diagonal streaks are the individual wave crests.

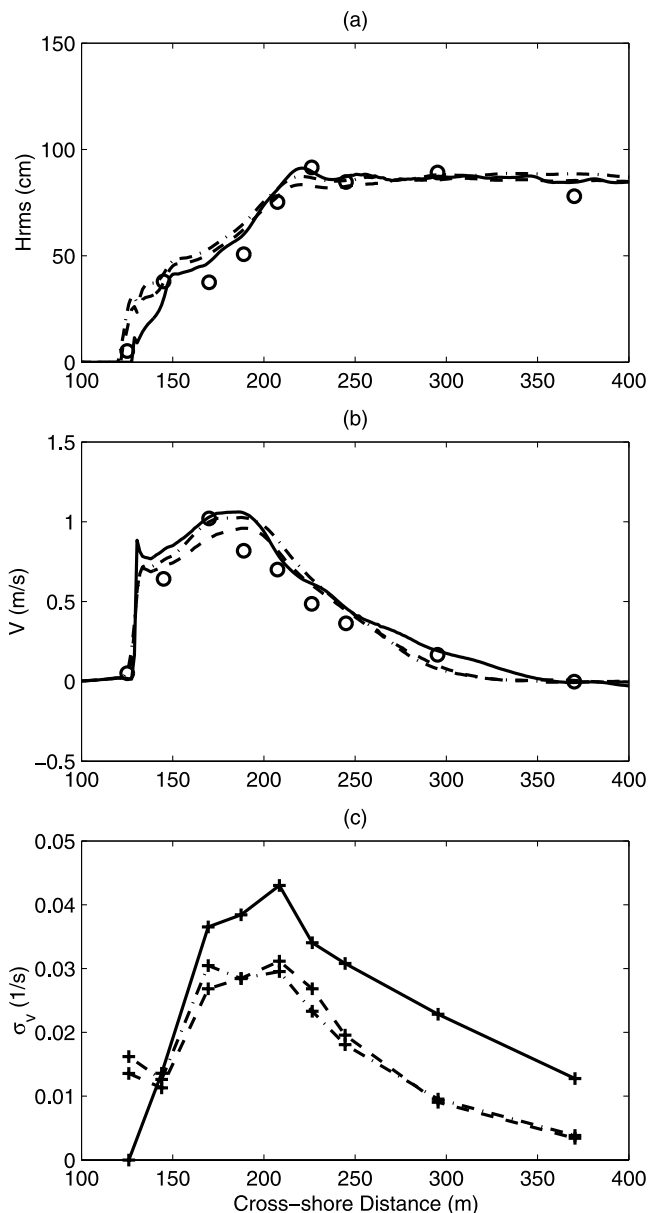


**Figure 19.** Comparisons of the computational results and the field measurements in the cases of regular waves (solid lines), narrow-banded spectrum (dot-dashed lines), and broadband spectrum (dashed lines): (a) root mean square wave height, (b) cross-shore distribution of longshore current, and (c) standard deviation of the instantaneous vorticity. Circles, measurements; and crosses, gage locations.

similar to the mixing effect of the breaking schemes based on the roller concept.

[62] We then apply the model to field conditions. The extended Boussinesq model predicts fairly well the root mean square wave height and mean longshore currents measured at Duck, North Carolina, during the DELILAH field experiment. Insight into the spatial and temporal variabilities of the wave-driven longshore currents and the associated vertical vorticity field under the phase-resolving wave forcing is given by the model results. It

is found that the propagation speed of the shear waves in the surf zone under field conditions is close to the velocity of the local, underlying current that advects the vertical vorticity. One interesting result of the simulations is the prediction of the strong longshore current shoreward of the bar crest as found in the field data. The fairly good model/data comparison is achieved when the cross-shore distribution of the bed shear stress coefficient is in keeping with the results of *Whitford and Thornton* [1996], based on the Superduck field experiment.

[63] Extensive numerical experiments are carried out to examine the response of the modeled longshore currents to the randomness of surface waves and the cross-shore distributions of bed shear stress coefficient. We find that both regular and irregular waves lead to very similar mean longshore currents, while the input of monochromatic, unidirectional waves results in much more energetic shear waves than does the input of random waves. Three types of cross-shore distribution of bottom friction coefficient are tested. The model results favor *Whitford and Thornton's* [1996] finding that the bed shear stress coefficient for the area offshore the bar is larger than that in the trough, as better agreement with the field data for both regular and irregular waves is found if such coefficients are used in the Boussinesq model.

[64] In conclusion, the Boussinesq approach with the embedded wave-current interaction and wave randomness provides us with an alternative to phase-averaged models for wave-induced nearshore circulation. Though the improvement of computational speed and the inclusion of undertow into the model are needed, the promising results given by the 2-D, time domain Boussinesq model allow for the use of the model as a new tool to investigate the interaction of shear waves with surface gravity waves, and to understand the effects of wave randomness and directional spreading on longshore currents. The model is currently being utilized to simulate the Sandyduck data set with an emphasis on shear instabilities [*Kirby et al.*, 2002]. Results will be reported on in the near future.

[65] **Acknowledgments.** This study has been supported by the Naval Research Laboratory through grant N00173-02-1-G905 (QC), and the National Oceanographic Partnership Program through grant N00014-99-1-1051 (JTK). The bathymetric and wave data were provided by the Field Research Facility of the U.S. Army Engineering Waterways Experiment Station Coastal and Hydraulic Laboratory. Permission to use the data is appreciated. Discussions with Andrew Kennedy and Francisco Sancho at the early stage of the project are also acknowledged.

## References

- Abbott, M. B., H. M. Petersen, and O. Skovgaard, On the numerical modeling of short waves in shallow water, *J. Hydraul. Res.*, 16, 173–203, 1978.
- Allen, J. S., P. A. Newberger, and R. A. Holman, Nonlinear shear instabilities of alongshore currents on plane beaches, *J. Fluid Mech.*, 310, 181–213, 1996.
- Basco, D. R., Surfzone currents, *Coastal Eng.*, 7, 331–355, 1983.
- Battjes, J. A., R. J. Sobey, and M. J. F. Stive, Nearshore circulation, in *The Sea, Ocean Eng. Sci.*, vol. 9, edited by B. Lemechaute et al., pp. 468–493, John Wiley, Hoboken, N. J., 1991.
- Birkemeier, W. A., C. E. Long, and K. K. Hathaway, DELILAH, DUCK94 & SandyDuck: Three nearshore field experiments, in *Coastal Engineering 1996: Proceedings of the Twenty-Fifth International Conference*, edited by B. L. Edge, pp. 4052–4065, Am. Soc. of Civ. Eng., Reston, Va., 1996.
- Birkemeier, W. A., C. Donoghue, C. E. Long, K. K. Hathaway, and C. F. Baron, 1990 DELILAH nearshore experiment: Summary report, *Tech. Rep.*, CHL-97-24, Am. Soc. of Civ. Eng., New York, 1997.

- Borgman, L. E., Directional spectrum estimation for the  $S_{xy}$  gages, technical report, U.S. Army Corp of Eng. Waterw. Exp. Stn., Vicksburg, Miss., 1984.
- Bouws, E., H. Gunther, W. Rosenthal, and C. L. Vincent, Similarity of the wind wave spectrum in finite depth water, *J. Geophys. Res.*, *90*, 975–986, 1985.
- Bowen, A. J., The generation of longshore currents on a plane beach, *J. Mar. Res.*, *27*, 206–215, 1969.
- Bowen, A. J., Rip currents. I. Theoretical investigations, *J. Geophys. Res.*, *74*, 5467–5478, 1970.
- Chen, Q., and I. A. Svendsen, Effects of cross-shore boundary condition errors in nearshore circulation modeling, *Coastal Eng.*, *48*, 243–256, 2003.
- Chen, Q., P. A. Madsen, H. A. Schäffer, and D. R. Basco, Wave-current interaction based on an enhanced Boussinesq approach, *Coastal Eng.*, *33*, 11–40, 1998.
- Chen, Q., P. A. Madsen, and D. R. Basco, Current effects on nonlinear interactions of shallow-water waves, *J. Waterw. Port Coastal Ocean Eng.*, *125*, 176–186, 1999a.
- Chen, Q., R. A. Dalrymple, J. T. Kirby, A. B. Kennedy, and M. C. Haller, Boussinesq modelling of a rip current system, *J. Geophys. Res.*, *104*, 20,617–20,637, 1999b.
- Chen, Q., J. T. Kirby, R. A. Dalrymple, A. B. Kennedy, and A. Chawla, Boussinesq modelling of wave transformation, breaking, and runup. II: 2D, *J. Waterw. Port Coastal Ocean Eng.*, *126*, 48–56, 2000.
- Church, J. C., and E. B. Thornton, Effects of breaking wave induced turbulence within a longshore current model, *Coastal Eng.*, *20*, 1–28, 1993.
- Dalrymple, R. A., Rip currents and their causes, paper presented at 16th International Conference on Coastal Engineering, Am. Soc. of Civ. Eng., Hamburg, Germany, 1978.
- Feddersen, F., R. T. Guza, S. Elgar, and T. H. C. Herbers, Alongshore momentum balances in the nearshore, *J. Geophys. Res.*, *103*, 15,667–15,676, 1998.
- George, R., R. E. Flick, and R. T. Guza, Observation of turbulence in the surf-zone, *J. Geophys. Res.*, *99*, 801–810, 1994.
- Gobbi, M., J. T. Kirby, and A. B. Kennedy, On the consistency of fully nonlinear Boussinesq models and their ability to predict vertical vorticity fields, in *Coastal Engineering 2000: Conference Proceedings*, edited by B. L. Edge, pp. 1321–1334, Am. Soc. of Civ. Eng., New York, 2000.
- Karambas, T. V., and C. A. Koutitas, A breaking wave propagation model based on the Boussinesq equations, *Coastal Eng.*, *18*, 1–19, 1992.
- Kennedy, A. B., Q. Chen, J. T. Kirby, and R. A. Dalrymple, Boussinesq modelling of wave transformation, breaking, and runup. I: 1D, *J. Waterw. Port Coastal Ocean Eng.*, *126*, 39–47, 2000.
- Kirby, J. T., Higher-order approximations in the parabolic equation method for water waves, *J. Geophys. Res.*, *91*, 933–952, 1986.
- Kirby, J. T., Nonlinear, dispersive long waves in water of variable depth, in *Gravity Waves in Water of Finite Depth*, edited by J. N. Hunt, pp. 55–126, Comput. Mech., Billerica, Mass., 1997.
- Kirby, J. T., Q. Chen, J. Noyes, S. Elgar, and R. T. Guza, Evaluation of Boussinesq model predictions of nearshore hydrodynamics, *Eos Trans. AGU*, *83*(47), Fall Meet. Suppl., OS62E-05, 2002.
- Kobayashi, N., E. A. Karjadi, and B. D. Johnson, Dispersion effects on longshore currents in surf zone, *J. Waterw. Port Coastal Ocean Eng.*, *123*, 240–248, 1997.
- Liu, P. L.-F., Model equations for wave propagations from deep to shallow water, *Adv. Coastal Ocean Eng.*, *1*, 125–158, 1994.
- Liu, P. L.-F., Recent advancement in modeling of breaking wave and sediment transport in surf zone, paper presented at 4th International Conference on Hydrodynamics, Int. Assoc. for Hydraul. Res., Yokohama, Japan, 2000.
- Longuet-Higgins, M. S., Longshore currents generated by obliquely incident sea waves, 1, *J. Geophys. Res.*, *75*, 6778–6789, 1970a.
- Longuet-Higgins, M. S., Longshore currents generated by obliquely incident sea waves, 2, *J. Geophys. Res.*, *75*, 6790–6801, 1970b.
- Longuet-Higgins, M. S., and R. W. Stewart, The changes in amplitude of short gravity waves on steady non-uniform currents, *J. Fluid Mech.*, *10*, 529–549, 1961.
- Madsen, P. A., and H. A. Schäffer, Higher order Boussinesq-type equations for surface gravity waves: Derivation and analysis, *Philos. Trans. R. Soc. London, Ser. A.*, *356*, 1–59, 1998.
- Madsen, P. A., and H. A. Schäffer, A review of Boussinesq-type equations for gravity waves, in *Adv. Coastal Ocean Eng.*, *5*, 1–94, 1999.
- Nwogu, O., Alternative form of Boussinesq equations for nearshore wave propagation, *J. Waterw. Port Coastal Eng.*, *119*, 618–638, 1993.
- Özkan-Haller, H. T., and J. T. Kirby, Nonlinear evolution of shear instabilities of the longshore current: A comparison of observations and computations, *J. Geophys. Res.*, *104*, 25,953–25,984, 1999.
- Putrevu, U., and I. A. Svendsen, Shear instability of longshore currents: A numerical study, *J. Geophys. Res.*, *97*, 7283–7303, 1992.
- Putrevu, U., J. Oltman-Shay, and I. A. Svendsen, Effect of alongshore nonuniformities on longshore current predictions, *J. Geophys. Res.*, *100*, 16,119–16,130, 1995.
- Rego, V. S., and C. F. Neves, A Boussinesq-type wave model with vertical shear, *Ocean Wave Measurement and Analysis: Proceedings of the Third International Symposium Waves 97*, edited by B. L. Edge et al., pp. 446–460, Am. Soc. of Civ. Eng., Reston, Va., 1997.
- Reniers, A. J. H. M., Longshore current dynamics, Ph.D. diss., Delft Univ. of Technol., Delft, Netherlands, 1999.
- Reniers, A. J. H. M., and J. A. Battjes, A laboratory study of longshore currents over barred and non-barred beaches, *Coastal Eng.*, *30*, 1–22, 1997.
- Ruessink, B. G., J. R. Miles, F. Feddersen, R. T. Guza, and S. Elgar, Modeling the alongshore current on barred beaches, *J. Geophys. Res.*, *106*, 22,451–22,463, 2001.
- Schäffer, H. A., P. A. Madsen, and R. A. Deigaard, A Boussinesq model for waves breaking in shallow water, *Coastal Eng.*, *20*, 185–202, 1993.
- Shen, C. Y., Constituent Boussinesq equations for waves and currents, *J. Phys. Oceanogr.*, *31*, 850–859, 2001.
- Slinn, D. N., J. S. Allen, P. A. Newberger, and R. A. Holman, Nonlinear shear instabilities of alongshore currents over barred beaches, *J. Geophys. Res.*, *103*, 18,357–18,379, 1998.
- Slinn, D. N., J. S. Allen, and R. A. Holman, Alongshore currents over variable beach topography, *J. Geophys. Res.*, *105*, 16,971–16,998, 2000.
- Smagorinsky, J., General circulation experiments with the primitive equations. I. The basic experiment, *Mon. Weather Rev.*, *91*, 99–165, 1963.
- Smith, J. M., M. Larson, and N. C. Kraus, Longshore current on a barred beach: Field measurements and calculation, *J. Geophys. Res.*, *98*, 22,717–22,731, 1993.
- Sørensen, O. R., H. A. Schäffer, and P. A. Madsen, Surf zone dynamics simulated by a Boussinesq-type model. III: Wave induced horizontal nearshore circulation, *Coastal Eng.*, *33*, 155–176, 1998.
- Svendsen, I. A., Analysis of surf zone turbulence, *J. Geophys. Res.*, *92*, 5115–5124, 1987.
- Svendsen, I. A., and U. Putrevu, Nearshore mixing and dispersion, *Proc. R. Soc. London, Ser. A*, *445*, 1–16, 1994.
- Svendsen, I. A., and U. Putrevu, Surf-zone hydrodynamics, *Adv. Coastal Ocean Eng.*, *2*, 1–78, 1995.
- Svendsen, I. A., K. Yu, and J. Veeramony, A Boussinesq breaking wave model with vorticity, *Coastal Engineering 1996: Proceedings of the Twenty-Fifth International Conference*, edited by B. L. Edge, pp. 1192–1204, Am. Soc. of Civ. Eng., Reston, Va., 1996.
- Svendsen, I. A., F. E. Sancho, J. Oltman-Shay, and E. B. Thornton, Modeling nearshore circulation under field conditions, *Ocean Wave Measurement and Analysis: Proceedings of the Third International Symposium Waves 97*, edited by B. L. Edge, pp. 765–776, Am. Soc. of Civ. Eng., Reston, Va., 1997.
- Thornton, E. B., Variation of longshore current across the surf zone, *Coastal Engineering (Proceedings of the 12th International Conference on Coastal Engineering)*, pp. 291–308, Am. Soc. of Civ. Eng., Reston, Va., 1970.
- Veeramony, J., and I. A. Svendsen, The flow in surf-zone waves, *Coastal Eng.*, *39*, 93–122, 2000.
- Visser, P. J., Laboratory measurements of uniform longshore currents, *Coastal Eng.*, *15*, 563–593, 1991.
- Wei, G., J. T. Kirby, S. T. Grilli, and R. Subramanya, A fully nonlinear Boussinesq model for surface waves. part 1: Highly nonlinear unsteady waves, *J. Fluid Mech.*, *294*, 71–92, 1995.
- Wei, G., J. T. Kirby, and A. Sinha, Generation of waves in Boussinesq models using a source function method, *Coastal Eng.*, *36*, 271–299, 1999.
- Whitford, D. J., and E. B. Thornton, Bed shear stress coefficients for longshore currents over a barred profile, *Coastal Eng.*, *27*, 243–262, 1996.
- Wu, C.-S., E. B. Thornton, and R. T. Guza, Waves and longshore currents: Comparison of a numerical model with field data, *J. Geophys. Res.*, *90*, 4951–4958, 1985.
- Yoon, S. B., and P. L.-F. Liu, Interaction of currents and weakly nonlinear water waves in shallow water, *J. Fluid Mech.*, *205*, 397–419, 1989.

Q. Chen, Department of Civil Engineering, University of South Alabama, Mobile, AL 36688, USA. (qchen@jaguar1.usouthal.edu)

J. T. Kirby and F. Shi, Center for Applied Coastal Research, University of Delaware, Newark, DE 19716, USA.

R. A. Dalrymple, Department of Civil Engineering, Johns Hopkins University, Baltimore, MD 21218, USA.

E. B. Thornton, Oceanography Department, Naval Postgraduate School, Monterey, CA 93943, USA.